nature communications

Article

https://doi.org/10.1038/s41467-025-62132-y

Metabolism archetype cancer cells induce protumor TREM2$^+$ macrophages via oxLDL-mediated metabolic interplay in hepatocellular carcinoma

Received: 12 August 2024

Accepted: 11 July 2025

Published online: 23 July 2025

Check for updates

Tianhao Chu[1,2,5], Guiqi Zhu[1,2,5], Zheng Tang[1,2,5], Weifeng Qu[1,2,5], Rui Yang[1,2], Haiting Pan[3], Yi Wang[1,2], Ruilin Tian[4], Leilei Chen[4], Zhiqi Guan[1,2], Yichao Bu[1,2], Qianfu Zhao[1,2], Jiafeng Chen[1,2], Shengwei Mao[1,2], Yuan Fang[1,2], Jun Gao[1,2], Xiaoling Wu[1,2], Jian Zhou[1,2], Weiren Liu[1,2] ✉, Dan Ye[4] ✉, Jia Fan[1,2] ✉ & Yinghong Shi[1,2] ✉

The functional programs adopted by cancer cells and their impact on the tumor microenvironment are complex and remain unclear. Here, we identify three distinct single-cell archetypes (i.e. metabolism, stemness and inflammation) in hepatocellular carcinoma (HCC) cells, each exhibiting unique spatial distribution. Further analysis shows an immune-suppressive niche populated by metabolism archetype cancer cells and TREM2-positive tumor-associated macrophages (TREM2$^+$ TAMs), which exacerbates immune exclusion and compromises patient outcomes. Mechanistically, we demonstrate that the upregulated squalene epoxidase (SQLE) expression in metabolism archetype cancer cells facilitates the generation of oxidized LDL (oxLDL). OxLDL induces TREM2$^+$ TAM polarization through the TREM2-SYK-CEBPα axis, enabling these TAMs to promote cancer cell invasion, resistance to effector cytokines and CD8$^+$ T cell dysfunction. Importantly, cancer cell-intrinsic SQLE and TREM2$^+$ TAMs are associated with inferior immunotherapy response in human and mouse HCC. Our results highlight an oxLDL-mediated metabolic interplay between cancer cells and TREM2$^+$ TAMs, offering a promising therapeutic avenue for HCC immunotherapies.

Hepatocellular carcinoma (HCC) is the fourth leading cause of cancer-related death worldwide[1]. Despite great advances in early detection and treatment strategies for HCC, the majority of patients are diagnosed at advanced stages, precluding surgical resection and resulting in a dismal 5-year survival rate below 20%[2]. Intratumoral heterogeneity (ITH) is a hallmark of HCC, profoundly influencing metastasis, recurrence, and resistance to treatment[3]. Recent studies applying high-dimensional, single-cell methods have fueled the understanding of tumor microenvironment (TME) heterogeneity in HCC[4]. However, exploration of the subtypes and functional programs adopted by HCC

[1]Department of Liver Surgery and Transplantation, Liver Cancer Institute, Zhongshan Hospital, Fudan University, Key Laboratory of Carcinogenesis and Cancer Invasion of Ministry of Education, Shanghai, China. [2]Research Unit of Liver cancer Recurrence and Metastasis, Chinese Academy of Medical Sciences, Beijing, China. [3]Endoscopy Center and Endoscopy Research Institute, Zhongshan Hospital, Fudan University, Shanghai, China. [4]Molecular and Cell Biology Lab, Institutes of Biomedical Sciences, Shanghai Medical College of Fudan University, Shanghai, China. [5]These authors contributed equally: Tianhao Chu, Guiqi Zhu, Zheng Tang, Weifeng Qu. ✉e-mail: liu.weiren@zs-hospital.sh.cn; yedan@fudan.edu.cn; fan.jia@zs-hospital.sh.cn; shi.yinghong@zs-hospital.sh.cn

cancer cells at the single-cell level remains limited, largely due to the technical challenges in capturing hepatocyte-lineage cells through single-cell RNA sequencing (scRNA-seq)[5,6]. While prior studies have proposed classification models pertaining to cancer cells[7] or cancer stem cells (CSCs)[8] in HCC, their investigations have been hindered by relatively small cell populations, leaving unanswered questions regarding the modulation of the TME by distinct cancer cell subpopulations.

The reprogramming of TME by cancer cells is crucial for suppressing anti-tumor immunity, fostering tumor proliferation and metastasis[9]. Aberrant metabolism within cancer cells can greatly influence the features of tumor metabolic microenvironment (TMME), including altered nutrient availability, hypoxia, and immunosuppressive metabolite production[10]. These changes impair the metabolic fitness of immune cells, hindering their proliferation, differentiation, and effector functions[10]. Notably, cancer cells often display a marked upregulation in lipid metabolism, a strategic move that not only caters to their proliferation demands but also manipulates stromal cells, like tumor-associated macrophages (TAMs), contributing to an immunosuppressive TME[11,12]. Understanding these metabolic interactions will provide new insights into potential therapeutic targets, which can restore normative metabolic function or enhance the metabolic fitness of immune cells to combat cancer effectively.

TREM2 (triggering receptor expressed on myeloid cells 2) is a TAM-specific cell surface receptor that functions as a lipid sensor with broad implications for lipid metabolism, immune reaction, and phagocytosis[13]. Previous studies have demonstrated an immunosuppressive role of TREM2$^+$ TAMs in multiple cancers[14]. TREM2$^+$ TAMs are noted for their high expression of immune inhibitory molecules and play a pivotal role in inducing the exhaustion of CD8$^+$T cells[15]. Nevertheless, the impact of TREM2$^+$ TAMs in HCC appears to be more complex and controversial. Reports indicated that the expansion of TREM2+ TAMs following transarterial chemoembolization (TACE) treatment in HCC may hinder the effector function of CD8$^+$ T cells[16]. Conversely, another study showed that the presence of fetal liver-like FOLR2$^+$CD163$^+$ TAMs, rather than TREM2$^+$ TAMs, was associated with increased immunosuppressive interactions[17]. Moreover, despite the recognized enrichment of TREM2$^+$ TAMs in HCC tumor tissues[17], their exact origin and the mechanisms driving their accumulation within the TME of HCC remain unclear.

In this work, we employ a comprehensive approach including single-nucleus RNA sequencing (snRNA-seq), scRNA-seq, and spatial transcriptomic sequencing to unveil the heterogeneity of HCC cancer cells and their impact on TME. Leveraging snRNA-seq, known for its improved performance in sequencing hepatocyte-linage cells[5,6], we identify three distinct functional archetypes (i.e., metabolism, inflammation, and stemness) within HCC cancer cells. Moreover, we highlight a co-localization pattern between metabolism archetype cancer cells and TREM2$^+$ TAMs that restrict immune infiltration. Mechanistically, we find that the upregulated SQLE, a pivotal cholesterol biosynthesis enzyme, in metabolism archetype cancer cells leads to oxLDL formation, subsequently inducing TREM2$^+$ TAM infiltration via the activation of the TREM2-SYK-CEBPα axis. Importantly, targeting either TREM2 or SQLE disrupts this metabolic crosstalk, reactivates anti-tumor immunity, and improves the immunotherapy efficacy in HCC.

Results

Integrative single-cell and nucleus transcriptomic atlas of hepatocellular carcinoma

To obtain a comprehensive transcriptomic landscape of HCC, we applied two single-cell genomic methods: (1) scRNA-seq on 8 primary HCC tumors and 4 adjacent normal tissues, as well as 7 mouse tumors from our established spontaneous HCC model[18] integrated with a previous published dataset covering 2 normal mouse livers[19], and (2) snRNA-seq on 12 primary HCC tumors integrated with a previous published dataset encompassing 2 adjacent normal tissues[20] (Fig. 1A). To enable integrated analysis of single-cell multi-omics data, we utilized scANVI[21] for batch correction, which has been shown to perform well on integrating strong batch while preserving underlying biological information[22] (Illustrated in Supplementary Fig. S1A). To this end, we classified 10 major cell types in both human and mouse single-cell data (Fig. 1B and Supplementary Fig. S1B, E) and found that snRNA-seq captured more hepatocytes while scRNA-seq performed better at detecting immunocytes (Supplementary Fig. S1C). We observed strong similarity between the transcriptome profiles of major cell types in mouse and human (SVM-predicted probability > 0.4) except for lymphocytes (T, NK, and B cells) (SVM-predicted probability < 0.4, Supplementary Fig. S1F). Notably, the proportions of monocytes/macrophages and hepatocytes were significantly upregulated in human and mouse HCC tissue compared to adjacent normal liver (Supplementary Fig. S1G), indicating pivotal roles of these cell types in shaping HCC TME.

Three functional archetypes of HCC cancer cells

Due to its higher capture rate of hepatocyte-lineage cells[5,6], we utilized snRNA-seq to investigate the functional programs adopted by HCC cancer cells. The origins of cancer cells were confirmed by inferring copy number variations (inferCNV) (Supplementary Fig. S2A). Our snRNA-seq data revealed higher total cancer cells, cancer cells per sample, and cancer cell fractions compared to other published scRNA-seq datasets (Supplementary Fig. S2B). To dissect coherent functional programs preferentially expressed by cancer cell subsets across patients, we employed non-negative matrix factorization (NMF) on our snRNA-seq data. This analysis uncovered eight metaprograms, reflecting common expression patterns across multiple tumors (Fig. 1C). The observed 8 metaprograms were further annotated using the top 50 genes ranked by NMF scores (Supplementary Fig. S2C and Supplementary Data 3). Correlation analysis of obtained metaprograms revealed four expression modules presented in human HCC, including (1) Metaprogram P1, P2, and P3 (metabolism); (2) Metaprogram P4 (proliferation); (3) Metaprogram P5 (inflammation); (4) Metaprogram P6, P7 and P8 (stemness), which showed strong correlation within program while followed co-exclusion patterns with each other (Fig. 1D). NMF analysis on cancer cells of scRNA-seq data revealed these four similar expression modules (Supplementary Fig. S2D). Furthermore, a similar correlation pattern was observed in the public scRNA-seq dataset (GSE149614) and HCC bulk transcriptomes (TCGA-LIHC) (Supplementary Fig. S2E).

Notably, across individual cancer cells, metabolism, stemness, and inflammatory modules exhibited aggregated yet co-exclusion distribution (Fig. 1E and Supplementary Fig. S2E, F). However, the proliferation module was found to be upregulated in both a subset of metabolism and stemness archetype cancer cells (Fig. 1E and Supplementary Fig. S2G), indicating that it represented a cell state that occurred in multiple cancer cell subtypes[23]. Therefore, the above findings identified three functional archetypes in HCC cancer cells, including the metabolism archetype displaying enhanced lipid (cholesterol/fatty acid), lipoprotein, and xenobiotic metabolism, the stemness archetype exhibiting higher protein translation, EMT, and stem cell signatures, and the inflammation archetype characterized by acute-phase and complement responses (Supplementary Fig. S2H). Principal component analysis (PCA) confirmed that cancer cells of different archetypes formed independent clusters (Fig. 1F). In accord, we validated cancer cell metaprograms in our spontaneous HCC mouse model by showing 7 metaprograms (NMF programs mP1-mP7) (Supplementary Fig. S3A and Supplementary Data 3). We found that mP1, mP2, mP3, mP4, and mP7 partially simulated their functional counterparts of P4 (Proliferation), P1, P3 (lipid metabolism), and P8 (cancer stemness) programs in human HCC, while mouse HCC lacked

https://doi.org/10.1038/s41467-025-62132-y

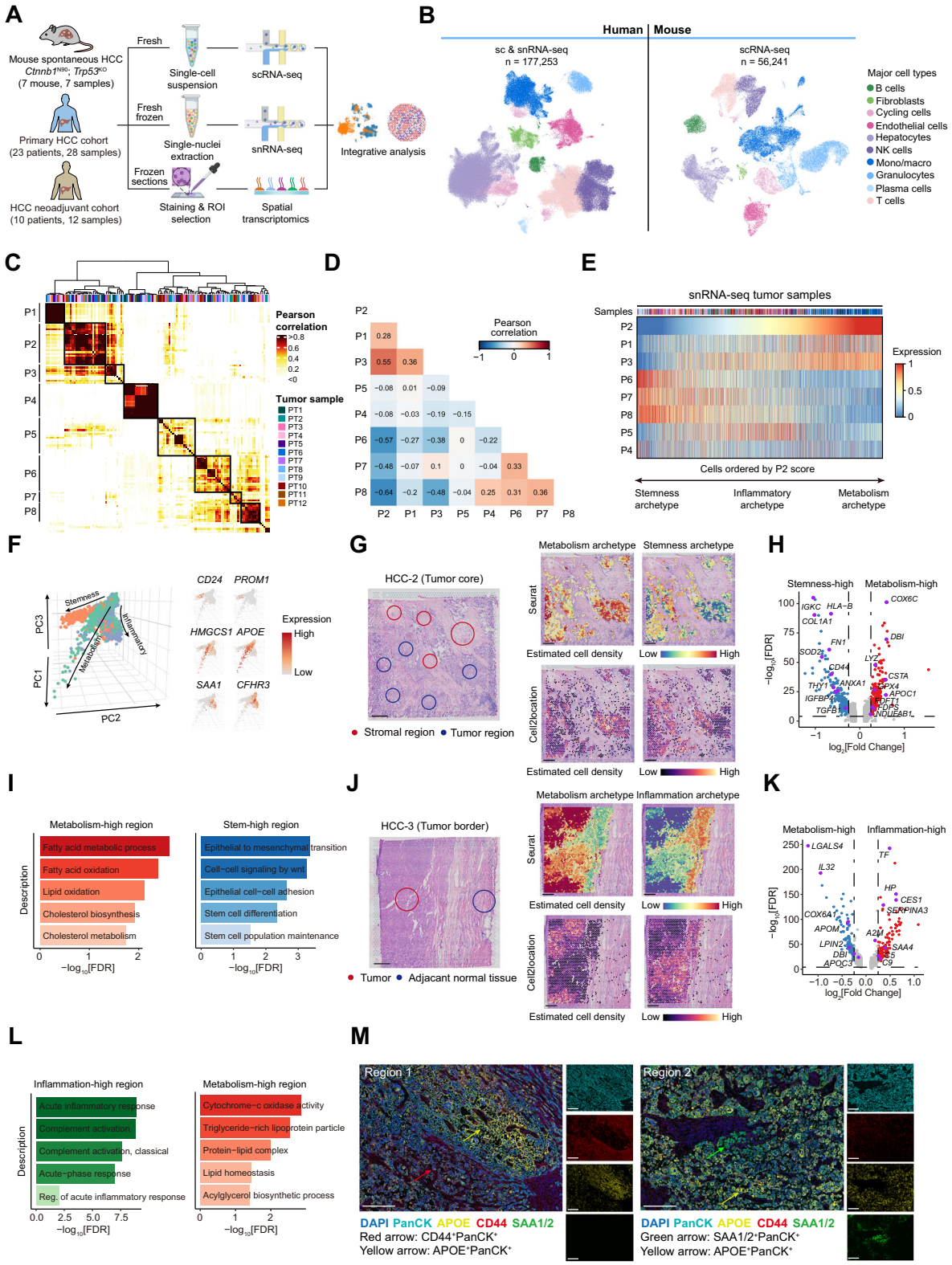

inflammatory response or a discrete EMT program as observed in HCC patients (Supplementary Fig. S3B).

To explore the spatial heterogeneity of these identified HCC archetypes, we integrated spatial transcriptomic data with our single-cell transcriptomic data using two different approaches: (1) spatial integration workflow implemented by the Seurat package[24]; (2) spatial deconvolution workflow implemented by the Cell2location package[25]. We performed spatial transcriptomics on 4 primary HCC tumors (Fig. 1A). Integration of spatial transcriptomics with snRNA-seq data revealed that functional archetypes exhibited distinct distribution patterns (Fig. 1G, J and Supplementary Fig. S3C). Further analysis showed that regions of different archetypes upregulated corresponding genes and GO terms observed in single-cell archetypes (Fig. 1H, I, K, L). The heterogeneous distribution of cancer cell archetypes was also confirmed by examining the mutually exclusive expressions of archetype-related markers in PanCK+ cancer cells (APOE

Fig. 1 | Three functional archetypes of HCC cancer cells. A Schematic diagram of this study design. **B** UMAP (uniform manifold approximation and projection) of main cell types in human primary HCC sc & snRNA-seq dataset (left) and mouse HCC scRNA-seq dataset (right). **C** Hierarchical clustering of pairwise similarities between NMF programs identified across all cancer cells from snRNA-seq samples. **D** Heatmap displays the Pearson correlation coefficients calculated between the single-cell gene signature scores of NMF metaprograms. **E** Heatmap showing the expression of NMF metaprograms. Cells were ordered by the P2 score. **F** PCA of 1000 random-sampled cancer cells colored by functional archetypes (left). The normalized, scaled expression of indicated marker genes for each functional archetype (right). **G**, **J** HE staining and predicted abundance of indicated cancer cell archetypes in spatial sections of HCC-2 (**G**) and HCC-3 (**J**). Data are representative of $n = 4$ spatial transcriptomic slides. Scale bar, 1 mm. **H**, **K** Volcano plot displays the DEGs between indicated spatial regions in HCC-2 (**H**) and HCC-3 (**K**). **I**, **L** GO analysis of the DEGs of indicated spatial regions in HCC-2 (**I**) and HCC-3 (**L**). **M** Immunofluorescence staining of CD44, APOE, SAA1/2, and PanCK on HCC sections. For each field, representative cells are indicated by arrows, including $CD44^+PanCK^+$ cells (red), $APOE^+PanCK^+$ cells (yellow), and $SAA1/2^+PanCK^+$ cells (green). Scale bar, 50 μm. Images are representative of $n = 3$ HCC samples. Schematic in **A** was created in BioRender. Chu, T. (2025) https://BioRender.com/r2v4jgs.

for metabolism, SAA1/2 for inflammation, and CD44 for stemness) (Fig. 1M). Furthermore, H&E staining revealed distinct pathological features of HCC archetypes: stemness archetype cells were characterized by spindle-shaped nucleus, indicating the upregulation of EMT process[26]; metabolism archetype cells had generally round nuclei and medium cell size; inflammation archetype cells were identified with increased cytoplasmic volume, which could be due to cell swelling that resulted from persistent inflammatory stress[27] (Supplementary Fig. S3D).

We next extended the archetype identification to human and mouse HCC cell lines. Analysis of the expression data of 31 human HCC cell lines (GSE97098) revealed that these cell lines can be classified into metabolism (9 cell lines) and stemness (22 cell lines) archetypes based on the archetype signature genes (Supplementary Fig. S3E), but no cell lines demonstrated prominent inflammatory archetype characteristics. Further, RNA sequencing on 4 mouse HCC cell lines revealed similar metabolism/stemness classification patterns (Supplementary Fig. S3F): Hepalclc7 and Hepa1-6 were classified as metabolism archetypes, with elevated expressions of apolipoprotein (*Apoa2, Apoc1*), xenobiotic (*Fmo3*) and fatty acid/cholesterol (*Fabp4, Hmgcr, Sqle*) metabolism, while RIL-175 and Hep53.4 showed closer relationships with stemness archetype, with elevated expressions of stemness-related genes (*Cd24a, Klf5*). Scoring analysis confirmed that cancer cell lines that belong to the metabolism archetype have higher expressions of metabolism-related NMF program (P1, P2, P3, mP3, mP4), while cancer cell lines of the stemness archetype upregulated stemness-related NMF program (P6, P8, mP7) (Supplementary Fig. S3G, H).

Together, our study unveils three distinct archetypes (metabolism, stemness, and inflammation) in HCC cancer cells, each exhibiting unique spatial distribution.

Identification of an immuno-inhibitory niche supported by metabolism archetype cancer cells and $TREM2^+$TAMs

During the development of human malignancies, genetically heterogeneous malignant cells have distinct interactions with the local microenvironment. To gain insights into the impact of HCC archetypes on the TME, we investigated the spatial co-localization of malignant cells with nonparenchymal cells, such as immune cells, endothelial cells, and fibroblasts. Re-clustering of non-malignant cells revealed 31 different cell subtypes (Fig. 2A and Supplementary Fig. S4A–C). Notably, Seurat spatial integration revealed that metabolism archetype cancer cells showed spatial co-localization with immunosuppressive TAMs, characterized by $TREM2^+$TAMs and $FOLR2^+$TAMs, while exhibiting spatial segregation with effector lymphocytes, such as $CD8^+$T effector memory (Tem), $CD4^+$T activated, and B cells (Fig. 2B, C and Supplementary Fig. 4D, E). A similar localization pattern was observed in public HCC spatial transcriptomic datasets (GSE224411, Supplementary Fig. S4F). Furthermore, across the tumor region in all four spatial transcriptomic samples, cancer cells of metabolism but not stemness or inflammation archetype exhibited strong spatial co-localization with $TREM2^+$TAMs (Fig. 2D and Supplementary Fig. 4G), suggesting that $TREM2^+$TAM formed an immunosuppressive niche specifically with metabolism archetype cancer cells. This niche was validated by cell2location spatial deconvolution, which demonstrated a similar colocalization of metabolism archetype cells and $TREM2^+$TAMs that restricted effector immune cell infiltration (Fig. 2E, F). Moreover, multiplex immunofluorescence (mIF) analysis confirmed this colocalization pattern of metabolism archetype cancer cells ($APOE^+PanCK^+$) and $TREM2^+$TAMs ($TREM2^+CD68^+$) at the protein expression level (Fig. 2G). Consistently, expression of macrophage and $TREM2^+$TAM signature genes was elevated in metabolism archetype-high regions (Supplementary Fig. S4H).

To validate and understand the role of this colocalization pattern in a larger patient cohort, we deconvoluted TCGA-LIHC bulk RNA-sequencing data with the BayesPrism algorithm[28]. Our results revealed that patients with higher metabolism archetype proportion exhibited increased $TREM2^+$TAM, decreased $CD8^+$T cell and $CD8^+$Tem infiltration (Supplementary Fig. S4I). Moreover, higher proportions of both metabolism archetype cancer cells and $TREM2^+$TAMs defined a subgroup of patients with shorter progression-free interval (PFI) and disease-free interval (DFI) (Supplementary Fig. S4J). In this subgroup, protumor myeloid infiltration was increased, but the infiltration of other TME cells was decreased, including lymphocytes and stromal cells (Supplementary Fig. S4K). These results suggested that the co-upregulation of $TREM2^+$TAMs and metabolism archetype cancer cells may promote immuno-suppressive TME formation and HCC progression.

Considering that this niche showed immuno-suppressive characteristics, we sought to investigate whether $TREM2^+$TAM, metabolism archetype cancer cells, and their co-localization were associated with HCC immunotherapy response. We established an HCC neoadjuvant cohort of 10 patients who underwent anti-PD1 therapy before surgical resection, followed by scRNA-seq (4 patients) and immunohistochemistry (10 patients) analysis (Fig. 1A and Supplementary Fig. S5A, B). To investigate the association between cancer cell heterogeneity and immunotherapy response in the context of cancer cell archetypes, we transferred the archetype annotation from snRNA-seq data to the cancer cells of immune checkpoint blockade non-responsive (ICB-NR) and ICB-responsive (ICB-R) tumors using Seurat reference mapping algorithms[24]. This method accurately identified the presence of metabolism and stemness archetype cancer cells in ICB-R/ICB-NR tumors, as evidenced by the expression of archetype-related markers (Supplementary Fig. S5C). However, only a limited number of cells (<10) were assigned to the inflammation archetype, likely due to the limited capture of cancer cells by scRNA-seq. Proportion analysis showed that the metabolism archetype of cancer cells is enriched in ICB-NR tumors (Supplementary Fig. S5D). Consistently, genes related to lipoprotein, xenobiotic, and fatty acid/cholesterol metabolism were upregulated in ICB-NR cancer cells (Supplementary Fig. S5E). Further analysis of the myeloid cells revealed that $TREM2^+$TAMs were significantly enriched in ICB-NR HCC (Supplementary Fig. S5F, G). Markers of $TREM2^+$TAMs, rather than those of other TAMs, were upregulated in TAMs of ICB-NR HCC (Supplementary Fig. S5H). The enrichment of metabolism archetype cancer cells and $TREM2^+$TAMs was validated in an independent HCC immunotherapy cohort containing bulk RNA-seq and $CD45^+$ scRNA-seq data (GSE235863)

https://doi.org/10.1038/s41467-025-62132-y

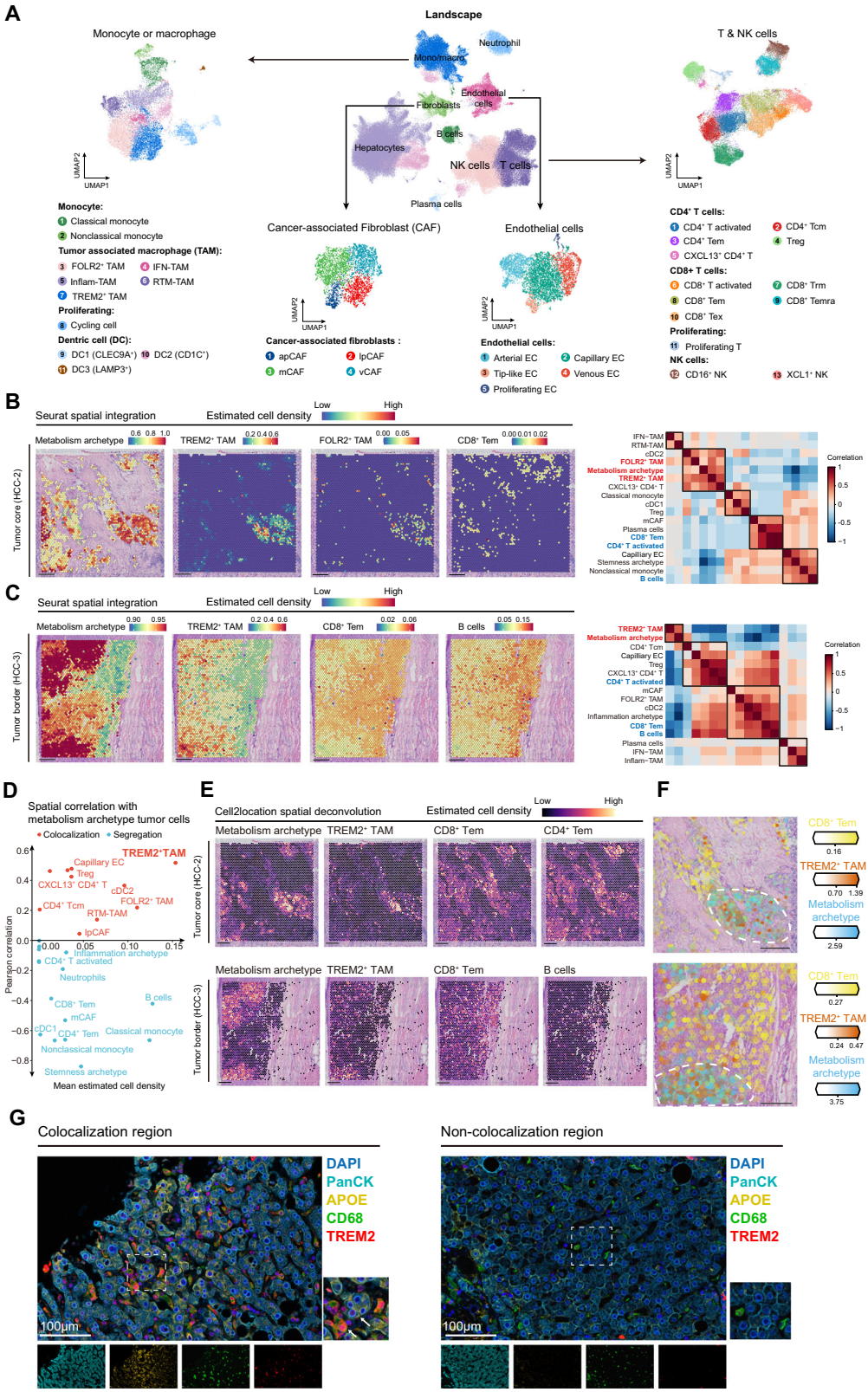

(Supplementary Fig. S5I). These data demonstrated the association of metabolism archetype cancer cells and TREM2$^+$TAMs with HCC immunotherapy resistance. Furthermore, we analyzed the spatial localization of metabolism archetype cancer cells and TREM2$^+$TAMs in ICB-R/ICB-NR samples by mIF analysis. Our results showed that the co-localization structure between TREM2$^+$TAMs and metabolism archetype cancer cells (APOE$^+$PanCK$^+$) is preserved in ICB-NR but not ICB-R HCC (Supplementary Fig. S5J). This observation was validated in a public spatial transcriptomic dataset[29], which revealed spatial co-expression of metabolism archetype and TREM2$^+$TAM signature genes in ICB-NR but not ICB-R samples, with notably decreased *CD8A* expression in this co-expression region (Supplementary Fig. S5K).

Taken together, our results indicate that metabolism archetype cancer cells support an immuno-inhibitory niche characterized by

Fig. 2 | Identification of an immuno-inhibitory niche supported by metabolism archetype cancer cells and TREM2⁺TAMs. A UMAP of main cell types and their subtypes recovered from the human sc & snRNA-seq dataset. **B**, **C** Seurat-predicted cell abundance of indicated cell subtypes on spatial sections of HCC-2 (**B**, left) and HCC-3 (**C**, left). Visualization of cell type co-localization by Pearson correlations in HCC-2 (**B**, right) and HCC-3 (**C**, right). Positive correlation values indicate spatial co-localization, while negative values represent spatial segregation. Scale bar, 1 mm. **D** Dotplot displays the mean estimated cell abundance (*x*-axis) and spatial correlation coefficients with metabolism archetype cancer cells (*y*-axis) of indicated cell clusters across the tumor region of four spatial transcriptomic slices in this study (HCC-1, HCC-2, HCC-3, and HCC-4). Positive correlation values indicate spatial co-localization, while negative values represent spatial segregation. **E** Cell2location-predicted cell abundance of indicated cell subtypes on spatial sections of HCC-2 (upper) and HCC-3 (lower). Scale bar, 1 mm. **F** Cell abundance for CD8⁺Tem, TREM2⁺TAM, and metabolism archetype cancer cells in HCC-2 (upper) and HCC-3 (lower), shown as overlaid color intensity over the hematoxylin and eosin (H&E) images. White dotted lines indicated the niche formed by metabolism archetype cancer cells and TREM2⁺TAMs that restricted CD8⁺Tem infiltration. Data are representative of $n = 4$ spatial transcriptomic slides. Scale bar, 1 mm. **G** Immunofluorescence staining of PanCK, APOE, CD68, and TREM2 on HCC tissue sections. Two images represented the colocalization region and non-colocalization region of metabolism archetype cancer cells and TREM2⁺TAMs, respectively. White arrows indicated the close proximity between metabolism archetype cancer cells (APOE⁺PanCK⁺) and TREM2⁺TAMs (CD68⁺TREM2⁺). Scale bar, 100 μm. Images are representative of $n = 3$ HCC samples.

increased myeloid cell infiltration, especially TREM2⁺TAMs, which promotes HCC progression and immunotherapy resistance.

TREM2⁺TAM drives HCC progression and immunotherapy resistance via SPP1-mediated dual action on CD8⁺T cells and cancer cells

We next examined the mechanisms of TREM2⁺TAMs in HCC progression and immunotherapy resistance. Scissor[30] prediciton analysis revealed that cells associated with worse clinical outcomes (Scissor⁺ cells) were mainly enriched in TREM2⁺TAMs (Fig. 3A). Correspondingly, TREM2⁺TAM was the only cluster that indicated worse clinical outcomes after adjusting for clinical variables in multivariable Cox survival analyses (Fig. 3B). These results indicated that TREM2⁺TAMs were more associated with HCC progression than other myeloid clusters.

To understand the transcriptional identities of cancer-promoting TAMs, we performed differential expression (DE) analysis of Scissor⁺ cells with other myeloid cells and found that SPP1 ranks the highest among the differential expressed genes (Fig. 3C and Supplementary Data 3). SPP1 is a glycoprotein secreted by cancer cells, CAFs, or macrophages, which plays a pivotal role in regulating cancer growth, drug resistance, and anti-tumor immunity[31,32]. Interestingly, TREM2⁺TAMs but not CAFs or cancer cells expressed the highest level of SPP1 in the HCC TME (Supplementary Fig. S6A), and TREM2 strongly correlated with SPP1 in TAMs but not normal macrophages (Fig. 3D), which was confirmed by mIF (Fig. 3E). Furthermore, single-cell proportion analysis and flow cytometry revealed that TREM2⁺SPP1⁺TAMs were significantly enriched in HCC tumor tissues (Supplementary Fig. S6B, C). Notably, in the TCGA-LIHC cohort, TREM2 and SPP1 expressions are strongly correlated in tumor samples (Supplementary Fig. S6D), and co-upregulation of TREM2/SPP1 was indicative of worse prognosis (Fig. 3F). Additionally, analysis of mouse HCC scRNA-seq revealed a similar tumor-specific TREM2⁺SPP1⁺TAM subset with conserved transcriptomic signatures across species (SVM-predicted probability > 0.4, Supplementary Fig. S6E–H). These results indicated that TREM2⁺TAM promoted HCC progression, possibly via SPP1 secretion.

We further confirmed that TREM2⁺TAM was the major source of SPP1 in our neoadjuvant cohort, and SPP1 expression was significantly upregulated in TAMs from ICB-NR HCC (Fig. 3G and Supplementary Fig. S6I). Similar results were obtained in CD45⁺ scRNA-seq data from GSE235863 (Supplementary Fig. S6J). Furthermore, spatial co-expressions of TREM2 and SPP1 were detected in ICB-NR but not ICB-R HCC (Supplementary Fig. S6K). Consistently, mIF confirmed that TREM2⁺SPP1⁺TAMs were enriched in ICB-NR HCC tissues (Supplementary Fig. S6L). These results supported that TREM2⁺TAM and its SPP1 production are upregulated in immunotherapy-resistant HCC. Moreover, we analyzed putative crosstalk of TREM2⁺TAM-derived SPP1 signaling using LIANA ligand-receptor analysis[30]. Our results revealed that SPP1-integrin interactions between TREM2⁺TAM and cancer cells, as well as SPP1-CD44 interactions between TREM2⁺TAM and CD8⁺T cells, were increased in ICB-NR HCC (Supplementary Fig. S6M). Analyzing expressions of SPP1 receptors confirmed that integrins and CD44 were upregulated in cancer cells and CD8⁺T cells from ICB-NR HCC, respectively (Fig. 3H). Notably, expressions of SPP1 and its receptors were enhanced in the niche supported by metabolism archetype cancer cells and TREM2⁺TAMs (Supplementary Fig. S6N), and co-expression of metabolism archetype-related markers, TREM2, SPP1, and SPP1 receptors, was detected in ICB-NR HCC (Supplementary Fig. S6O). Previous reports suggested that SPP1-CD44 is an important immune checkpoint restricting CD8⁺T cell activation[33], while SPP1-integrin signaling is crucial for cancer cell survival, invasion, and treatment resistance[34]. Therefore, TREM2⁺TAM-secreted SPP1 acting on cancer cells and CD8⁺T cells could play a role in supporting immunosuppressive niche formation and immunotherapy resistance in HCC (Fig. 3I).

Next, we sorted TREM2⁺/TREM2⁻ TAMs from fresh human HCC samples, followed by co-culture assays with CD8⁺T cells or cancer cells (Supplementary Fig. S7A). Cancer cell line resembling metabolism archetype signatures (Hep3B) was used to model the in vivo co-localization of metabolism archetype cancer cells and TREM2⁺TAMs. Isolated TREM2⁺TAMs expressed markers resembling the TREM2⁺TAM subset in single-cell data (*SPP1*, *MSR1*, *FABP5*, *CTSB*, etc.) (Fig. 3J) and upregulated SPP1 mRNA and protein expressions (Supplementary Fig. S7B, C). Co-culture assays with CD8⁺T demonstrated that TREM2⁺TAMs hindered IFNγ⁺CD8⁺T expansion, which can be reversed by SPP1 neutralization (Fig. 3K), suggesting that TREM2⁺TAM-derived SPP1 is a mediator of CD8⁺T dysfunction. Furthermore, co-culture assays with Hep3B showed that TREM2⁺TAMs promoted cancer cell proliferation, migration, and invasion in an SPP1-dependent manner, confirming that TREM2⁺TAM-derived SPP1 promoted HCC progression (Supplementary Fig. S7D, E). Additionally, TREM2⁺TAM co-culture did not affect the expression of metabolism archetype signature genes (Supplementary Fig. S7F), suggesting that the cancer-promoting effect of TREM2⁺TAMs was not contingent upon shaping the metabolic phenotype of cancer cells.

IFNγ and TNF (IFNγ/TNF) are two CD8⁺T-cell effector cytokines that play an important role in anti-tumor immunity, and resistance of cancer cells to IFNγ/TNF-mediated apoptosis contributes to immunotherapy resistance[35]. We found that despite the enrichment of immunosuppressive TREM2⁺TAMs, *TNF*/*IFNG* expressions of CD8⁺T cells were upregulated in ICB-NR tumors (Fig. 3L), consistent with previous reports[36]. *TNF* and *IFNG* expressions were mainly restricted to effector CD8⁺T clusters (CD8⁺Teff, early CD8⁺Tem, and CXCL13⁺CD8⁺T) (Fig. 3M), which were mostly enriched in ICB-NR tumors (Fig. 3N). This phenomenon suggested the ongoing cytokine elaboration in ICB-NR HCC, which could be due to the failure of tumor control and continuing tumor-elicited inflammation[37]. Considering that SPP1 mediated cancer cell treatment resistance, we examined whether TREM2⁺TAM-derived SPP1 induced the resistance of cancer cells to IFNγ/TNF-mediated apoptosis. Hep3B co-cultured with TREM2⁺TAMs exhibited decreased sensitivity to combined treatment of TNF/IFNγ, which was reversed by SPP1 neutralization (Fig. 3O).

https://doi.org/10.1038/s41467-025-62132-y

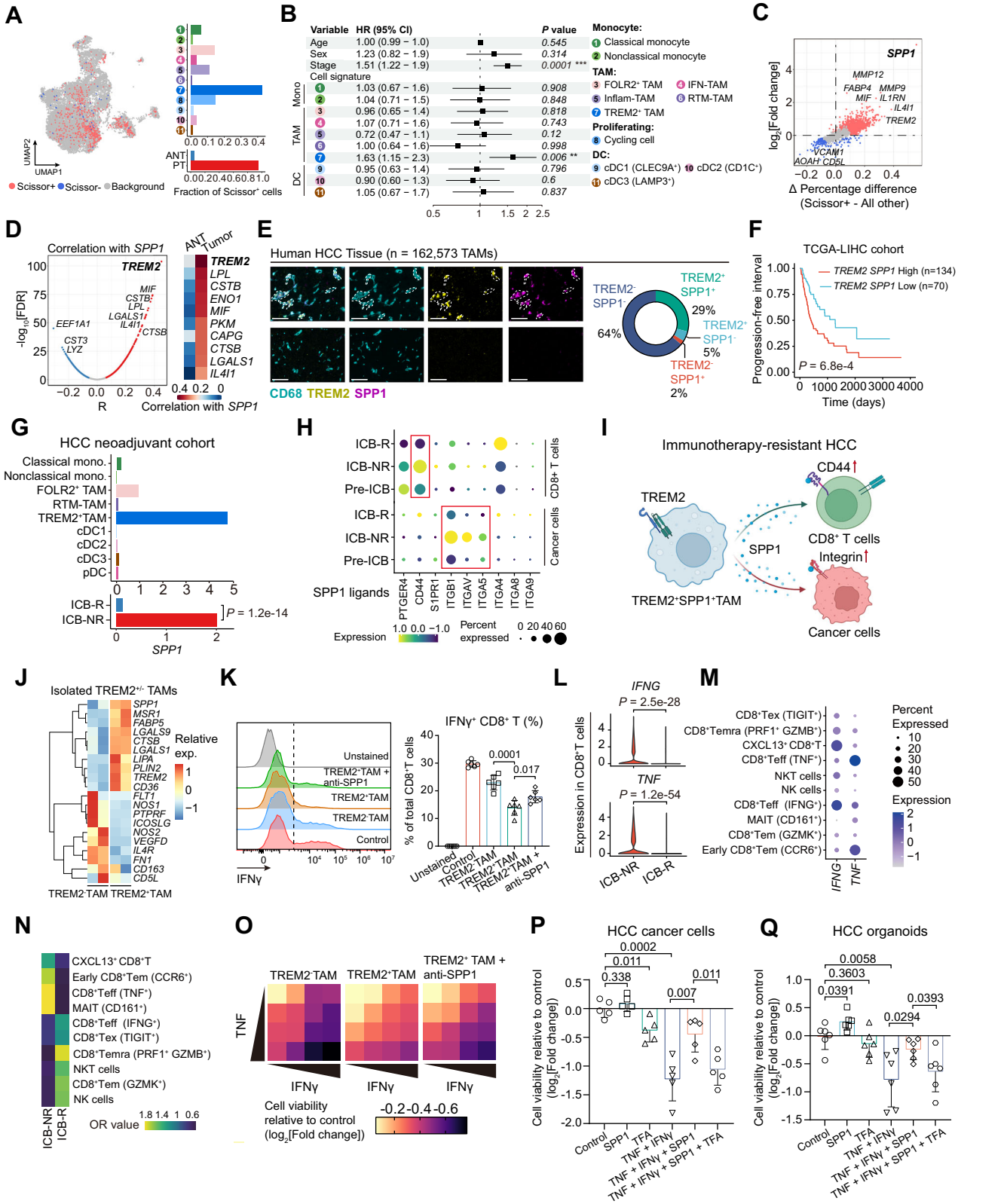

Furthermore, recombinant SPP1 drove the resistance to TNF/IFNγ in cultured cancer cells and HCC organoids, which can be reversed by integrin inhibitors (Fig. 3P, Q), suggesting SPP1-integrin interaction as an important mechanism for the resistance of cancer cells to TNF/IFNγ-mediated cell death.

To validate the function of TREM2$^+$SPP1$^+$TAMs in vivo, we isolated TREM2$^+$/TREM2$^-$TAMs from our spontaneous HCC tumors and performed co-injection experiments with Hepa1–6 cells, which better simulated the transcriptional identities of metabolism archetype cancer cells (Supplementary Fig. S3F). TREM2$^+$TAMs promoted tumor growth in immunocompetent C57/BL6 mice (Supplementary Fig. S7G), which was associated with increased intratumoral SPP1$^+$TAMs and decreased effector CD8$^+$T cells (Supplementary Fig. S7H, I). Cancer cells isolated from TREM2$^+$TAM co-injection tumors exhibited

Fig. 3 | TREM2⁺TAM drives HCC progression and immunotherapy resistance via SPP1-mediated dual action on CD8⁺T cells and cancer cells. A UMAP of the Scissor-selected cells (left). Barplot shows the distribution of Scissor⁺ cells across different myeloid populations and conditions (right). **B** Forestplot shows the hazard ratios and 95% confidence intervals for different myeloid cluster signatures and clinical information according to a multivariable Cox model in the TCGA-LIHC cohort ($n = 353$ patients). Squares represent the hazard ratios, and the horizontal bars extend from the lower limits to the upper limits of the 95% confidence intervals of the estimates of the hazard ratios. **C** Dotplot displays the DEGs between Scissor⁺ cells and all other cells. **D** Dotplot displays the expression correlation of *SPP1* with other genes in myeloid cells (left). Heatmap shows the expression correlation of indicated genes with *SPP1* in myeloid cells from adjacent non-tumor (ANT) and tumor samples (right). **E** Representative images and quantification of TREM2, SPP1, and CD68 immunofluorescence staining on human HCC sections. Representative cells that denote the co-upregulation of TREM2 and SPP1 in CD68⁺ TAMs are circled by a dotted line. Scale bar, 50 μm. **F** Kaplan–Meier survival analysis of HCC patients from the TCGA-LIHC cohort categorized into groups based on normalized *TREM2* and *SPP1* expression. The cutpoints for patient grouping were calculated by the surv_cutpoint function from the survminer R package. **G** Barplot shows the mean expression of SPP1 across different myeloid cell populations (upper) and in TAMs from ICB-R and ICB-NR HCC samples (lower). **H** Dotplot shows the expression of SPP1 ligands in CD8⁺T cells (above) or cancer cells (below) from pre-ICB, ICB-NR, and ICB-R HCC scRNA-seq samples. **I** Schematic of the interaction between TREM2⁺TAMs and CD8⁺T cells or cancer cells in immunotherapy-resistant HCC. **J** Heatmap shows the relative expression of indicated genes in isolated TREM2⁺/TREM2⁻ TAMs. **K** Flow cytometry of IFNγ expression in CD8⁺T cells co-cultured with human HCC-isolated TREM2⁻TAMs or TREM2⁺TAMs ± SPP1 antibody (1 μg/mL). CD8⁺T cells were isolated from human PBMC and then activated with anti-CD3/CD28 + IL-2 (50 U/mL) before co-culture assays. **L** Violin plots display the expression of *IFNG* and *TNF* in CD8⁺T cells from ICB-NR or ICB-R scRNA-seq samples, with two-tailed Wilcoxon-test statistics. **M** Dotplot shows the relative expression of *IFNG* and *TNF* in CD8⁺T cell clusters. **N** Tissue preference of CD8⁺T cell clusters, revealed by odds ratio (OR) value. **O** Relative cell viability (mean of $n = 3$ biological replicates) for Hep3B cells treated with a half-log dilution series of TNF (2.5–250 ng/mL) and IFNγ (1–100 ng/mL), cocultured with human HCC-isolated TREM2⁻TAMs or TREM2⁺TAMs ± SPP1 antibody (1 μg/mL). **P** Relative cell viability of Hep3B cells treated with mock, SPP1 (50 ng/mL), integrin inhibitor TFA (100 μM), TNF (250 ng/mL) plus IFNγ (100 ng/mL) (TNF/IFNγ), TNF/IFNγ plus SPP1, or TNF/IFNγ plus SPP1 plus TFA (100 μM) for 24 h. **Q** Relative cell viability for patient-derived HCC organoid with indicated treatment. Data represent the mean ± SD, $n = 5$ biological replicates in (**P**), $n = 6$ biological replicates in (**K**, **Q**). Statistical significance was determined by two-tailed Wald test (**B**), two-tailed unpaired *t* test (**K**, **P**, **Q**), two-tailed Wilcoxon signed rank test (**L**), and log rank test (**F**). Schematic in **I** was created in BioRender. Chu, T. (2025) https://BioRender.com/r2v4jgs. Source data are provided as a Source Data file.

decreased sensitivity to IFNγ/TNF treatment (Supplementary Fig. S7J). Additionally, TREM2⁺TAMs enhanced tumor growth in immunodeficient NOD-SCID *Il2rγ*$^{-/-}$ (NSG) mice (Supplementary Fig. S7K) and increased tumoral Ki67 expression (Supplementary Fig. S7L). Furthermore, considering that different cancer cell archetypes were observed in mouse spontaneous HCC, we established the *Trem2*-deficient spontaneous HCC model to investigate the effect of TREM2⁺TAM on cancer growth and immunotherapy efficacy in the context of tumor heterogeneity (Supplementary Fig. S7M). We found that *Trem2*-deficient mice exhibited increased sensitivity to anti-PD1 (Supplementary Fig. S7N). *Trem2* deficiency decreased SPP1 expression of TAMs and showed an addictive effect on activating CD8⁺T cells with anti-PD1 (Supplementary Fig. S7O, P). Moreover, treatment of SPP1 antibody reduced tumor growth in wild-type but not *Trem2*-deficient mice (Supplementary Fig. S7Q), confirming that TREM2⁺TAM-derived SPP1 is crucial for HCC immunosuppression and tumor progression.

Overall, our findings highlight the role of TREM2⁺TAMs in promoting tumor progression and immunotherapy resistance via SPP1-mediated dual action on HCC cancer cells and CD8⁺T cells.

TREM2⁺TAMs exhibit elevated lipid metabolism and are induced by oxLDL produced from metabolism archetype cancer cells

To gain more mechanistic insights into the co-localization of metabolism archetype cancer cells and TREM2⁺TAMs, we examined but failed to find any specific ligand-receptor pairs between these two cell types (Supplementary Fig. S8A). Given that the modulation of local TMME by cancer cells potentially influences immune cell functions[10], we hypothesized that local TMME affected by metabolism archetype cancer cells might reprogram TREM2⁺TAM polarization. Indeed, metabolite flux estimation (FLUXestimator)[38] revealed an upregulation of lipid-related metabolic flux and metabolites in the regions with co-localization of TREM2⁺TAMs and metabolism archetype cancer cells (Supplementary Fig. S8B, C). Furthermore, TREM2⁺TAMs were enriched in lipid metabolism, oxidative phosphorylation, and endocytosis program but depleted of immune response GO terms (Fig. 4A, B), resembling lipid-associated macrophages (LAMs)[39]. Besides, TREM2⁺TAMs exhibited high levels of LAM signatures but low levels of M1/M2 signatures (Supplementary Fig. S8D). These results thus indicate a potential role of lipids in inducing TREM2⁺TAM polarization in the TME.

For validation, primary macrophages were cultured with tumor interstitial fluid (TIF) isolated from fresh HCC samples, representing the metabolite profile of TME, followed by determining the expression of TREM2 and SPP1, two markers of TREM2⁺TAMs. We found that HCC-derived TIF was enriched in lipid-related metabolites (Supplementary Fig. S8E). Furthermore, HCC-derived TIF potently induced the expression of TREM2 and SPP1 in macrophages, which was attributed to lipids, but not lactate acid (Fig. 4C and Supplementary Fig. S8F, G). In addition, the co-localization of TREM2 and SPP1 expression and Bodipy staining was readily detected in HCC tissue sections (Fig. 4D), reaffirming that lipids induced TREM2⁺TAM polarization.

To further investigate which lipid component(s) induce TREM2⁺TAM polarization, we examined the effect of diverse lipids or lipoproteins, known to be enriched in TIF[40], on regulating TREM2 and SPP1 expressions in TAMs generated by an in vitro induction system (Fig. 4E and Supplementary Fig. S8H). Our data demonstrated that oxLDL most potently induced the expression of TREM2 and SPP1 as well as SPP1 secretion in TAMs (Fig. 4E). This effect of oxLDL on inducing TREM2 and SPP1 expression was in a dose-dependent manner (Fig. 4F). As a result, oxLDL-treated TAMs promoted invasion, proliferation, resistance to TNF/IFNγ of Hepa1-6 cells, and inhibited CD8⁺T cell activation in a SPP1-dependent manner (Fig. 4G, H and Supplementary Fig. S8I, J). In accord, oxLDL was the most upregulated lipoprotein in HCC TIF (Fig. 4I and Supplementary Fig. S8K), and tumor interstitial levels of oxLDL (Fig. 4J), but not other lipoproteins (Supplementary Fig. S8L), were positively correlated with TREM2⁺SPP1⁺TAM infiltration in human HCC samples. Similar results were observed in the mouse spontaneous HCC model (Fig. 4K, L). Furthermore, RNA sequencing revealed a distinct transcriptomic shift triggered by oxLDL but not LDL treatment in TAMs (Fig. 4M). DE analysis showed that oxLDL-induced genes were over-represented in the single-cell transcriptome of TREM2⁺TAMs (Fig. 4N and Supplementary Fig. S8M). Moreover, we co-injected mock/oxLDL-treated in vitro-induced TAMs with Hepa1–6 cells (Fig. 4O), and found that oxLDL-treated TAMs promoted tumor growth (Fig. 4P), which was associated with increased intratumoral TREM2⁺SPP1⁺TAMs (Fig. 4Q) and decreased IFNγ⁺CD8⁺T cell infiltration (Fig. 4R). Additionally, given that heterogeneous cancer cell modules were observed in our spontaneous HCC model (Supplementary Fig. S3A, B) and tumor-derived organoid is a powerful approach to replicate intratumoral heterogeneity[41], we further constructed co-injection models of mock/oxLDL-treated TAMs with spontaneous HCC-derived organoid to validate above findings in the context of cancer cell heterogeneity. Our data showed that oxLDL-treated TAMs promoted organoid growth,

https://doi.org/10.1038/s41467-025-62132-y

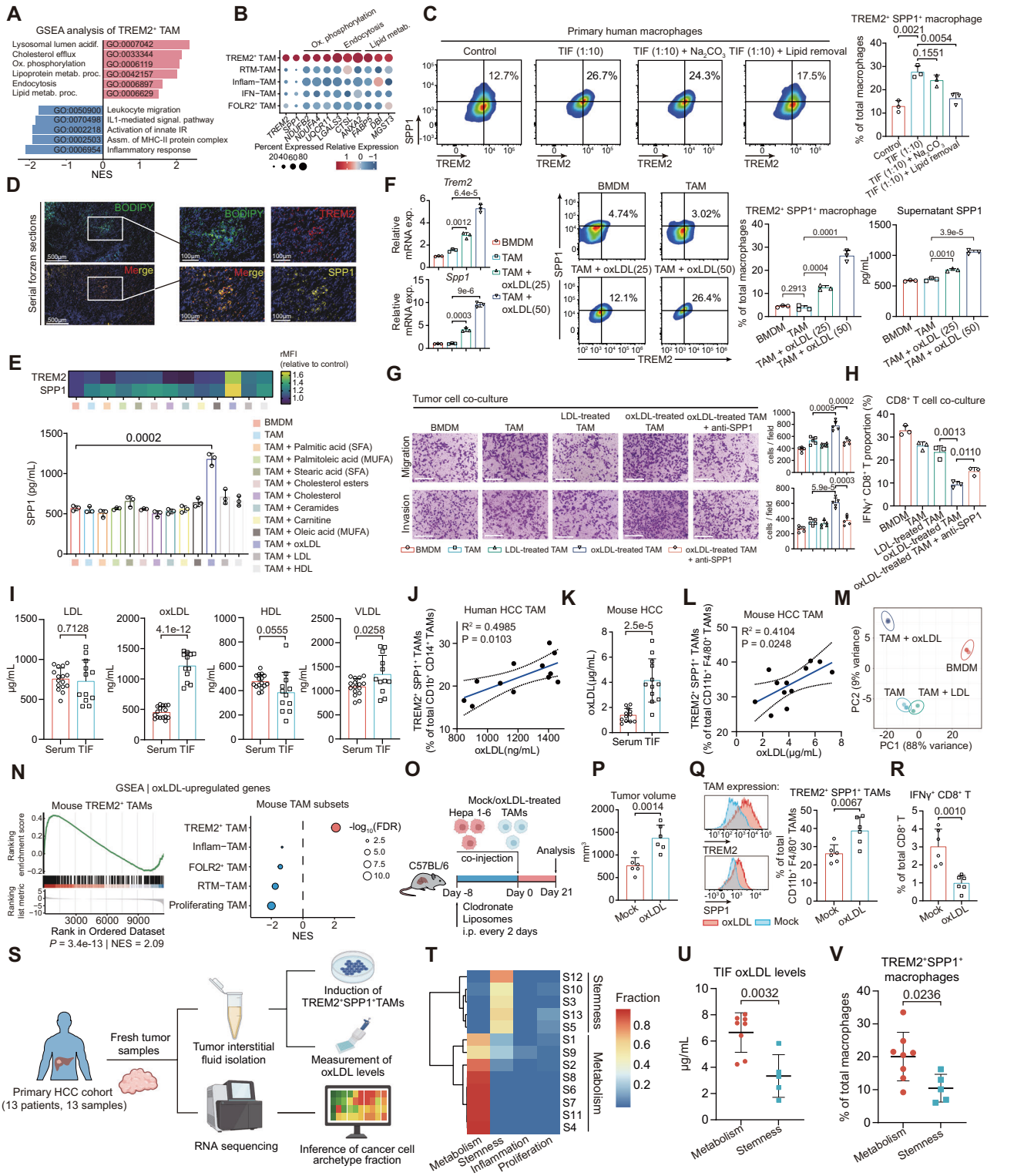

increased intratumoral TREM2$^+$SPP1$^+$TAMs, and decreased IFNγ$^+$GZMB$^+$CD8$^+$T infiltration (Supplementary Fig. S8N–P). These results confirmed oxLDL as a TMME factor capable of eliciting the protumor TREM2$^+$TAM state in HCC.

We next investigated whether the metabolism archetype of cancer cells was associated with oxLDL production and the following TREM2$^+$TAM expansion. The formation of oxLDL requires lipid peroxidation, which is induced by deregulated lipid metabolism and increased oxidative stress in cancer[42]. We found that lipid peroxidation-associated genes and oxidative stress response signatures were elevated in metabolism archetype cancer cells and their enriched spatial region (Supplementary Fig. S9A–C). Cancer cell lipid peroxidation score was also positively associated with TREM2$^+$TAM infiltration in the snRNA-seq dataset (Supplementary Fig. S9D). To validate the association between metabolism archetype cancer cells and oxLDL production, we used in vitro-cultured Hepa1–6 and Hep53.4 to model the metabolism and stemness archetype cancer cells. RNA sequencing revealed increased expression of oxidative stress response and lipid peroxidation-related genes in Hepa1–6 cells (Supplementary Fig. S9E). Further analysis showed that Hepa1–6 had

Fig. 4 | TREM2 + TAMs exhibit elevated lipid metabolism and are induced by oxLDL produced from metabolism archetype cancer cells. A Gene set enrichment analysis (GSEA) on genes ranked by log2 fold change between TREM2$^+$TAMs and other TAM clusters. **B** Dotplot shows the expression of selected genes belonging to the indicated biological process in TAM subsets. **C** Flow cytometry of TREM2 and SPP1 expression in macrophages treated with TIF ± Na_2CO_3 or lipid removal reagent (Cleanascite). **D** Bodipy, TREM2, and SPP1 staining on HCC frozen sections. Scale bar, 500 μm (left), 100 μm (right). Images are representative of $n = 2$ HCC samples. **E** Heatmap summarizing TREM2, SPP1 expression (mean of $n = 3$ biological replicates, upper) and supernatant SPP1 concentrations (lower) in BMDMs or TAMs treated with indicated lipids. **F** Relative *TREM2*, *SPP1* mRNA (left), protein expression (middle), and supernatant SPP1 concentration (right) in BMDM or TAM treated with vehicle or oxLDL (25 or 50 μg/mL). **G** Transwell migration and evasion assays of Hepa1–6 co-cultured with BMDM or TAM treated with vehicle, LDL (50 μg/mL) or oxLDL (50 μg/mL) ± SPP1 antibody (1 μg/mL). Scale bar, 100 μm. Quantification was performed with $n = 5$ random fields. **H** Flow cytometry of IFNγ expression in CD8$^+$T cells co-cultured with BMDM or TAM treated with vehicle, LDL, or oxLDL ± SPP1 antibody. **I**, **K** Concentrations of indicated lipoproteins in human plasma ($n = 16$ patients) or human TIF ($n = 12$ patients) (**I**), and in mouse plasma or mouse TIF ($n = 12$ mice) (**K**). **J**, **L** Correlation between TIF oxLDL level and TREM2$^+$SPP1$^+$TAM proportion in human HCC tumors ($n = 12$) (**J**) and mouse HCC tumors ($n = 12$) (**L**). **M** PCA of the transcriptome of BMDM ($n = 3$ biological replicates) or TAM treated with vehicle ($n = 3$ biological replicates), LDL ($n = 2$ biological replicates), or oxLDL ($n = 3$ biological replicates). **N** GSEA of genes upregulated by oxLDL (log2 fold change > 1), on genes ranked by log2 fold change between TAM subsets versus other TAMs. Statistical *P* value was determined from 10,000 permutations. **O** Schematic of co-injection experiments. **P** Tumor volume of mock/oxLDL-treated TAM co-injection tumors ($n = 6$ mice). **Q**, **R** Flow cytometry of TREM2, SPP1 expression in TAMs (**Q**) and IFNγ expression in tumor-infiltrating CD8$^+$T cells (**R**) ($n = 6$ mice). **S** Schematic of the sample collection and analysis workflow. **T** Heatmap depicts the BayesPrism-inferred fractions of indicated cancer cell subpopulations in 13 HCC samples. Hierarchical clustering shows that these 13 HCC samples can be classified into metabolism (8 samples) and stemness (5 samples) subtypes. **U** OxLDL concentrations (mean of $n = 3$ experimental replicates) in the TIF isolated from metabolism ($n = 8$) and stemness ($n = 5$) subtype HCC samples. **V** Flow cytometry of TREM2 and SPP1 expression in macrophages (mean of $n = 3$ biological replicates) treated with TIF (1:10) isolated from metabolism ($n = 8$) and stemness subtype ($n = 5$) HCC samples. Data represent the mean ± SD, $n = 3$ biological replicates in (**C**, **E**, **F**, **H**). Statistical significance was determined by a two-tailed unpaired *t*-test (**C**, **E**–**I**, **K**, **P**–**R**, **U**, **V**) and a two-tailed one-sample *t*-test (**J**, **L**). Schematics in **O** and **S** were created in BioRender. Chu, T. (2025) https://BioRender.com/r2v4jgs. Source data are provided as a Source Data file.

upregulated lipid peroxidation and oxLDL production levels than Hepa53.4 and normal hepatocytes (AML12) in vitro (Supplementary Fig. S9F, G). Furthermore, orthotopic tumors of Hepa1–6 showed elevated oxLDL expression and TREM2$^+$TAM infiltration than those of Hepa53.4 or adjacent liver (Supplementary Fig. S9H, I). These results supported the role of the metabolism archetype of cancer cells in the activation of the oxLDL-TREM2$^+$TAM axis. To extend the above findings to humans, we demonstrated similar elevation of lipid peroxidation levels and oxLDL production in Hep3B compared to MHCC97H cells (Supplementary Fig. S9J). Moreover, we collected a cohort of 13 HCC samples, followed by TIF isolation and paired RNA sequencing analysis (Fig. 4S). These samples were classified into metabolism and stemness subtypes based on the fractions of metabolism and stemness archetype cancer cells (Fig. 4T), which were confirmed by the expressions of metabolism and stemness-related NMF programs (Supplementary Fig. S9K). Notably, we found that TIF isolated from metabolism-subtype HCCs had elevated oxLDL levels (Fig. 4U and Supplementary Fig. S9L), and could more potently induce TREM2$^+$SPP1$^+$TAM expansion (Fig. 4V and Supplementary Fig. S9M). Additionally, mIF on serial sections of HCC tissue confirmed the upregulation of oxLDL levels and TREM2$^+$TAM infiltration in the metabolism archetype-enriched region (R1) but not the stemness archetype-enriched region (R2) (Supplementary Fig. S9N). These results suggested that the metabolism archetype of cancer cells was associated with oxLDL production and the following TREM2$^+$TAM expansion in HCC.

Together, our findings uncover tumor-enriched oxLDL as a TMME factor capable of eliciting the protumor TREM2$^+$TAM state in HCC. Furthermore, the metabolism archetype of cancer cells was associated with increased oxLDL production and the following TREM2$^+$TAM expansion.

OxLDL induces TREM2 and SPP1 expression via the TREM2/SYK/CEBPα axis in TAMs

ScRNA-seq data from wildtype and *Trem2*$^{-/-}$ tumors[14] demonstrated repressed expression of *Spp1* in *Trem2*$^{-/-}$ TAMs (Fig. 5A), which is consistent with our observation in *Trem2*$^{-/-}$ HCC (Supplementary Fig. S7N). We therefore assumed that TREM2 may participate in oxLDL sensing to regulate SPP1 expression and subsequent secretion. To test this hypothesis, we treated wildtype and *Trem2*$^{-/-}$ TAMs with oxLDL, and found that loss of *Trem2* hindered the effect of oxLDL on inducing SPP1 mRNA and protein expression (Fig. 5B). *Trem2*$^{-/-}$ TAMs failed to upregulate SPP1 expression in response to oxLDL (Supplementary Fig. S10A), and they were less potent in promoting T cell dysfunction and cancer cell invasion under oxLDL stimulation (Fig. 5C, D). Furthermore, oxLDL-induced SPP1 expression in wild-type TAMs was hindered by pre-incubating oxLDL with recombinant TREM2 protein or pre-treating TAMs with TREM2 blocking antibody (Supplementary Fig. S10B), confirming the crucial role of oxLDL-TREM2 interaction in controlling SPP1 expression. RNA-sequencing analysis revealed that *Trem2*$^{-/-}$ TAMs exhibited upregulation of marker genes that resemble liver resident macrophages (*Macro*, *Cd5l*, *Vcam1,* etc.; over-represented in RTM-TAMs), and downregulation of genes involved in lipid metabolism (*Lpl*, *Ldlr*, *Fabp3*, etc.; over-represented in TREM2$^+$TAMs) (Supplementary Fig. S10C, D). These results indicated that TREM2 deficiency could induce TAM to polarize from LAM-like to RTM-like under oxLDL stimulation.

Upon ligand binding, TREM2 recruits SYK via DAP12, leading to SYK phosphorylation[13]. To determine whether oxLDL stimulates TREM2 signaling, we examined and found that oxLDL treatment could dose-dependently increase the phospho-SYK (pSYK) levels in TAMs (Fig. 5E and Supplementary Fig. S10E). Conversely, in vitro-induced and in vivo-isolated *Trem2*$^{-/-}$ TAMs exhibited decreased pSYK levels (Fig. 5F, G). Treatment with SYK inhibitors (R406 or Piceatannol) could reverse the effect of oxLDL on inducing SPP1 expression in TAMs (Fig. 5H), reaffirming that oxLDL-stimulated TREM2-SYK signaling upregulates SPP1 expression in TAMs.

Activation of SYK regulates multiple transcription factors (TFs) that modulate cellular responses. By utilizing SCENIC to infer TF activation in TAM subsets, we identified three TFs (i.e., CEBPα, BHLHE41, and PBX3) that were upregulated in both human and mouse TREM2$^+$TAMs (Fig. 5I). Further analysis revealed that loss of *Cebpa* showed the most prominent effect on compromising the induction of *Trem2* and *Spp1* (Fig. 5J). Notably, CEBPα was one of the most upregulated TFs in TAMs compared to normal macrophages (Supplementary Fig. S10F). Full-length CEBPα (42 kDa, p42) was dose-dependently upregulated by oxLDL in in vitro-induced TAMs (Fig. 5K and Supplementary Fig. S10G). In contrast, CEBPα expression was decreased in *Trem2*$^{-/-}$ TAMs (Fig. 5L), as well as in TAMs treated with Syk inhibitors (Supplementary Fig. S10H). According to these findings, we next set out to check whether CEBPα controls TREM2 and SPP1 transcription in TAMs. Analysis of *Trem2* and *Spp1* gene promoters revealed predicted CEBPα binding sites (Supplementary Fig. S10I), which could be confirmed by chromatin immunoprecipitation-qPCR (ChIP-qPCR) analysis (Supplementary Fig. S10J). By introducing the binding sites into a luciferase reporter system, we showed that the luciferase activity was

https://doi.org/10.1038/s41467-025-62132-y

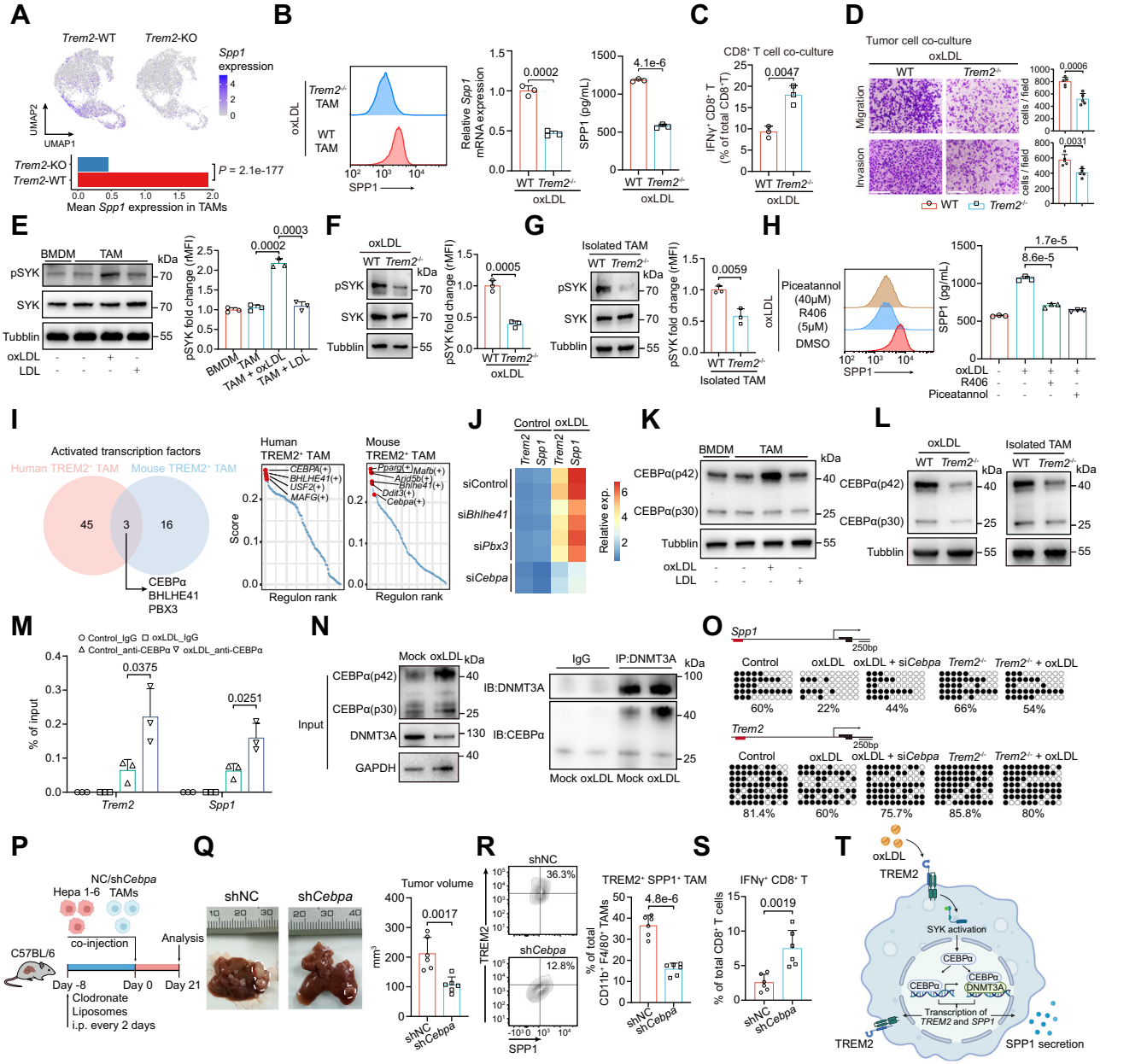

Fig. 5 | OxLDL induces TREM2 and SPP1 expression via the TREM2/SYK/CEBPα axis in TAMs. A UMAP projection (upper) and barplot (lower) show *Spp1* expression in TAMs from *Trem2*-wildtype or *Trem2*-KO tumors, with two-tailed Wilcoxon-test statistics. **B** Relative *SPP1* protein (left, representative of $n = 3$ biological replicates), mRNA (middle), and supernatant (right) expression in wildtype or *Trem2*$^{-/-}$ TAMs treated with oxLDL (50 μg/mL). **C** Flow cytometry of IFNγ in CD8$^+$T cells co-cultured with wildtype or *Trem2*$^{-/-}$ TAMs treated with oxLDL. **D** Transwell migration and evasion assays of Hepa1–6 co-cultured with wildtype or *Trem2*$^{-/-}$ TAMs treated with oxLDL. Scale bar, 100 μm. Quantification was performed with $n = 5$ random fields. **E**–**G** Western blot (WB) and flow cytometry of pSYK expression in BMDM or TAM treated with vehicle, LDL (50 μg/mL) or oxLDL (**E**), in wildtype or *Trem2*$^{-/-}$ TAMs treated with oxLDL (**F**), and in TAMs isolated from wildtype or *Trem2*$^{-/-}$ tumors (**G**). **H** Protein (left, representative of $n = 3$ biological replicates) and supernatant (right) expression of SPP1 in TAMs treated with oxLDL ± R406 (5 μM) or Piceatannol (40 μM). **I** Venn diagram shows the overlapping activated TFs in human and mouse TREM2$^+$TAM (left). Regulon ranks of top enriched TFs in human and mouse TREM2$^+$TAM (right). **J** Heatmap summarizing the qPCR results in TAMs treated with vehicle or oxLDL with indicated TF KD (mean of $n = 3$ biological replicates). **K**, **L** WB of CEBPα levels in BMDM or TAM treated with vehicle, LDL or oxLDL (**K**), in wildtype or *Trem2*$^{-/-}$ TAMs treated with oxLDL (**L**, left), and in TAMs isolated from wildtype or *Trem2*$^{-/-}$ tumors (**L**, right). **M** ChIP-qPCR assays of CEBPα binding at the *Trem2* or *Spp1* promoter ($n = 3$ experimental replicates). **N** Co-immunoprecipitation assays of DNMT3A and CEBPα interaction in TAMs treated with vehicle or oxLDL. **O** 5mC levels at the CpG-rich promoter regions of *Trem2* and *Spp1* were determined by BS-PCR in wildtype or *Trem2*$^{-/-}$ TAMs treated with vehicle or oxLDL ± si*Cebpa*. **P** Schematic of the co-injection experiments. **Q** Tumor volume of Hepa1-6 cells co-injected with shNC/sh*Cebpa* TAMs ($n = 6$ mice). **R**, **S** Flow cytometry of TREM2, SPP1 expression in TAMs (**R**) and IFNγ expression in tumor-infiltrating CD8$^+$T cells (**S**) ($n = 6$ mice). **T** Schematic summarizing the mechanism of oxLDL inducing TREM2 and SPP1 expression in TAMs. WB results shown were representative of three independent experiments in (**E**–**G**, **K**, **L**, **N**). Data represent the mean ± SD, $n = 3$ biological replicates in (**B**, **C**, **E**–**H**). Statistical significance was determined by the Wilcoxon signed rank test (**A**) and two-tailed unpaired *t* test (**B**–**H**, **M**, **Q**–**S**). Schematics in **P** and **T** were created in BioRender. Chu, T. (2025) https://BioRender.com/r2v4jgs. Source data is provided as a Source Data file.

upregulated by *Cebpa* overexpression but downregulated by mutation of CEBPα binding sites (Supplementary Fig. S10K). Furthermore, we observed that CEBPα occupancy at the promoter regions of *Trem2* and *Spp1* gene loci could be enhanced by oxLDL treatment in TAMs (Fig. 5M). We previously reported that CEBPα regulates gene expression via binding to and inhibiting DNMT3A[43]. Indeed, co-immunoprecipitation (co-IP) showed that the interaction of endogenous CEBPα and DNMT3A proteins was increased by oxLDL in TAMs (Fig. 5N). As a result, DNMT activity (Supplementary Fig. S10L) and global DNA methylation (Supplementary Fig. S10M) were suppressed in oxLDL-treated TAMs, which was diminished by *Cebpa* knockdown. Bisulfite (BS)-PCR and sequencing analysis showed that oxLDL treatment could decrease 5mC levels at the CpG-rich promoter regions of *Trem2* and *Spp1*, and this effect was, however, abolished by *Cebpa* or *Trem2* knockdown (Fig. 5O). Furthermore, *Cebpa* was depleted in in vitro-induced TAMs via lentiviral transduction of shRNA (Supplementary Fig. S10N), followed by co-injection with Hepa1–6 cells (Fig. 5P). We found that sh*Cebpa* TAMs were less potent in promoting tumor growth (Fig. 5Q), which was associated with decreased intratumoral TREM2$^+$SPP1$^+$TAMs (Fig. 5R) and increased IFNγ$^+$CD8$^+$T cell infiltration (Fig. 5S). Similar results were observed in the co-injection models of shNC/sh*Cebpa* TAMs with spontaneous HCC-derived organoid (Supplementary Fig. S10O–Q).

In summary, our results suggest that the TREM2-SYK-CEBPα axis is required for oxLDL-induced TREM2 and SPP1 transactivation in TAMs, elucidating a mechanistic pathway underlying TREM2$^+$SPP1$^+$TAM polarization and its impact on tumor progression (Fig. 5T).

Targeting SQLE enzyme enhances anti-tumor immunity by acting on the oxLDL-TREM2$^+$TAM axis

We next sought to find potential targets in metabolism archetype cancer cells to impair their action on oxLDL-TREM2$^+$TAM axis and cancer progression. Integrative survival analysis on 73 metabolism archetype-specific metabolism genes revealed that cholesterol metabolism-related genes (*SQLE*, *HMGCR*, *HMGCS1*, *FDFT1*) exhibited significant association with survival outcomes in multiple HCC cohorts (Fig. 6A). These genes were highly expressed in metabolism archetype cancer cells and corresponding spatial regions (Supplementary Fig. S11A, B), and showed tumor-specific expression (Supplementary Fig. S11C, D). Furthermore, the cholesterol metabolism activity of cancer cells was correlated with cancer cell lipid peroxidation and TREM2$^+$TAM infiltration in our snRNA-seq dataset (Supplementary Fig. S11E), suggesting dysregulated cholesterol metabolism of cancer cells as a potential target to impair the oxLDL-TREM2$^+$TAM axis.

We next selected SQLE, a rate-limiting enzyme in cholesterol metabolism, as the intervention target because of its strong association with HCC patient survival (Fig. 6A). Previous studies reported that SQLE induced intracellular NADPH/NADP$^+$ reduction and oxidative stress, which is essential for lipid peroxidation and subsequent oxLDL formation[44]. Furthermore, SQLE inhibition resulted in intracellular squalene accumulation, which is a natural antioxidant that prevents oxLDL accumulation[44]. Therefore, SQLE might be a crucial upstream regulator of the oxLDL-TREM2$^+$TAM axis in metabolism archetype cancer cells. Consistent with this notion, SQLE expression in cancer cells was positively correlated with TREM2$^+$TAM infiltration (Fig. 6B) rather than other TAM signatures (Supplementary Fig. S11F). IHC and mIF further showed a positive relationship of tumoral SQLE expression with oxLDL and TREM2$^+$SPP1$^+$TAM infiltration (Fig. 6C), and revealed a spatial co-localization between SQLE^{high} cancer cells, oxLDL, and TREM2$^+$TAMs on HCC sections (Supplementary Fig. S11G). Notably, single-cell and IF analysis showed upregulation of SQLE expression in ICB-NR cancer cells (Fig. 6D, E). These data indicated the role of SQLE in regulating the oxLDL-TREM2$^+$TAM axis and immunosuppressive microenvironments of HCC.

To explore the potential mechanism for SQLE reshaping the TME, *Sqle* was depleted in Hepa1–6 cells by shRNA (Supplementary Fig. S11H). As expected, depletion of *Sqle* led to decreased NADP$^+$/NADPH ratio and intracellular ROS (Fig. 6F), as well as repressed lipid peroxidation (Fig. 6G) and reduced oxLDL production (Fig. 6H). Interestingly, sh*Sqle* increased the uptake of Dil-labeled oxLDL by cancer cells (Fig. 6I), which was associated with upregulation of CD36 (Supplementary Fig. S11I), a major receptor responsible for oxLDL uptake. Treatment with CD36 inhibitor (Sulfo-N-succinimidyl oleate, SSO) reversed the elevated uptake of oxLDL in sh*Sqle* cancer cells (Fig. 6I). It is likely that the enhanced oxLDL uptake may compensate for the repression of de novo lipogenesis due to *Sqle* knockdown (Supplementary Fig. S11J). These results thus indicate that the intrinsic SQLE expression within cancer cells influences lipid peroxidation and the uptake of oxLDL, resulting in altered oxLDL levels within the TME (Supplementary Fig. S11K).

To further validate our findings in vivo, we constructed orthotopic mouse HCC models with *Sqle* knockdown (Fig. 6J). Our data demonstrated that sh*Sqle* tumors exhibited decreased growth compared to control cells (Fig. 6K). TIF-derived oxLDL levels were reduced by *Sqle* knockdown (Fig. 6L). Depletion of *Sqle* in cancer cells inhibited TREM2$^+$SPP1$^+$TAMs infiltration and promoted CD8$^+$T cell activation (Fig. 6M, N). Additionally, oxLDL levels were found to be positively correlated with TREM2$^+$TAMs while negatively correlated with IFNγ$^+$CD8$^+$T cells (Supplementary Fig. S11L, M). Despite the limited growth of sh*Sqle* tumors in immunodeficient NSG mice, the inhibition rate was lower than that in the immunocompetent model (Supplementary Fig. S11N), suggesting that retard tumor growth in sh*Sqle* tumors involves the alteration of immune response.

Finally, we investigated the effect of targeting SQLE on immunotherapy efficacy. Our data from the orthotopic HCC mouse model demonstrated an additive effect of sh*Sqle* and anti-PD1 on suppressing tumor growth (Fig. 6O, P). *Sqle* inhibition, but not anti-PD1, repressed TREM2$^+$SPP1$^+$TAM infiltration (Fig. 6Q). The combination of sh*Sqle* and anti-PD1 showed the highest efficacy in upregulating effector CD8$^+$ T cells (Fig. 6R). Importantly, administration of an FDP-approved SQLE inhibitor, terbinafine, in spontaneous HCC mouse models showed a combinatory effect with anti-PD1 against tumor growth (Fig. 6S, T). The tumoricidal effect of terbinafine and anti-PD1 was associated with decreased tumor interstitial oxLDL (Supplementary Fig. S11O), decreased TREM2$^+$SPP1$^+$TAMs (Fig. 6U), and elevated effector CD8$^+$T cells (Fig. 6V). Additionally, terbinafine treatment did not affect TREM2$^+$SPP1$^+$TAM proportion in response to oxLDL stimulation (Supplementary Fig. S11P), excluding the possibility that SQLE inhibition directly affects TREM2$^+$TAM polarization.

Taken together, our findings highlight the role of cancer cell-intrinsic SQLE in remodeling tumor immunity by modulating oxLDL levels and TREM2$^+$TAM infiltration in the TME, suggesting SQLE is a potential target to enhance immunotherapy efficacy in HCC.

Discussion

Increasing evidence suggests the complex heterogeneity and phenotypic variations within HCC. For instance, previous proteomic analyses identified three HBV-HCC subgroups (metabolism, proliferation, and microenvironment dysregulated)[45]. Likewise, transcriptomic analysis has uncovered three HCC subtypes: inflammatory, metabolic, and immunosuppressive[46]. Another study through transcriptomics has identified five HCC subtypes, highlighting that two subtypes with pronounced stem cell characteristics exhibit increased vascular invasion and poorer outcomes[47]. Our observation supports and extends these findings by identifying that metabolism, stemness, and inflammation co-exist as opposite cellular archetypes within HCC cancer cells, with proliferation acting as a common trait across multiple subpopulations of cancer cells. Distinct from previous bulk-level investigations, our work contributes to the understanding of heterogeneity

https://doi.org/10.1038/s41467-025-62132-y

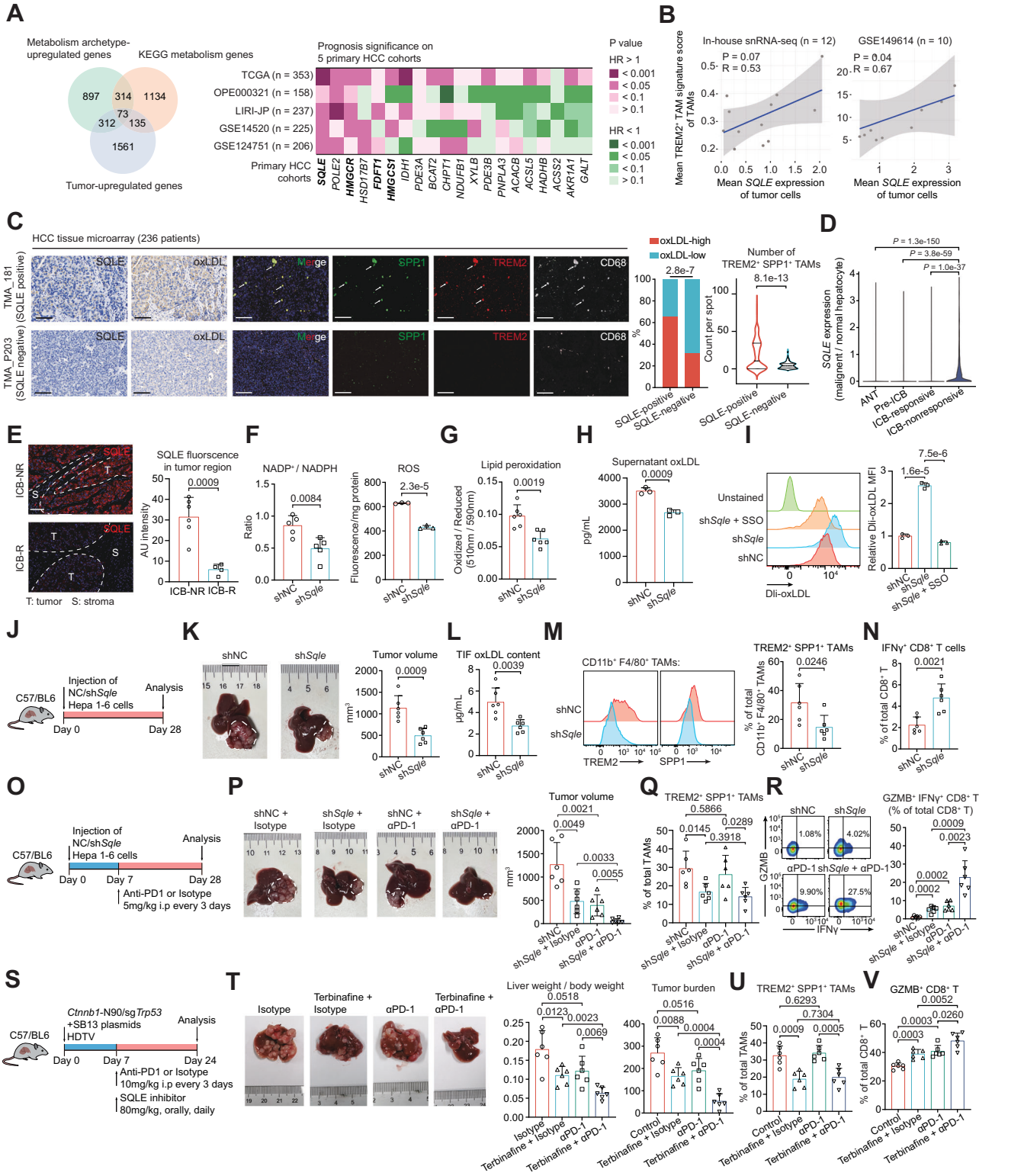

within HCC cancer cells at single-cell resolution, highlighting that metabolism, inflammation, and stem-cell reprogramming act as concert events in cancer cells to affect HCC progression. Furthermore, through the integration of multi-omics data, we demonstrated that heterogeneous malignant cell populations formed distinct niches with other non-malignant stromal cells. Except for the co-localization of metabolism archetype cancer cells and TAMs, our data showed that stemness archetypes tended to localize with CAFs and ECs, while the inflammation archetype was associated with the infiltration of lymphocytes (Fig. 2B, C). Nevertheless, how stemness and inflammation archetypes influence HCC progression is not well investigated in this study and requires further exploration.

The interaction between cancer cells and non-cancer cells within the TME through metabolic pathways is critical for influencing antitumor immunity and cancer progression[10]. Supporting this notion, enhanced lipogenesis activity in cancer cells can create a lipid-rich microenvironment, leading to M2-like TAM polarization[48] and myeloid-derived suppressor cell (MDSC) expansion[49]. In this study, we

Fig. 6 | Targeting SQLE enzyme enhances anti-tumor immunity by acting on the oxLDL-TREM2$^+$TAM axis. A Venn diagram shows the overlapping metabolism genes that are upregulated in the tumor and the metabolism archetype (left). Heatmap depicts prognostic significance of top genes in five primary HCC cohorts using an univariate Cox regression model (right). **B** Correlation between cancer cell SQLE expression and TREM2$^+$TAM signatures of TAMs in snRNA-seq ($n = 12$, left) and public scRNA-seq dataset ($n = 10$, right). **C** Representative images showing the expression of SQLE, oxLDL, TREM2, SPP1, and CD68 in SQLE-positive and SQLE-negative tissue spots from HCC TMA. Representative cells that denote the presence of TREM2$^+$SPP1$^+$TAMs are indicated by arrowheads. Scale bar, 50 μm (left). Composition of oxLDL-high or oxLDL-low spots in SQLE-positive ($n = 110$) and SQLE-negative ($n = 126$) spots. Quantification of TREM2$^+$SPP1$^+$TAMs in SQLE-positive and SQLE-negative spots (right). **D** Violinplot shows SQLE expression in normal/malignant hepatocytes from indicated groups, with two-tailed Wilcoxon-test statistics. **E** Representative images showing SQLE expression in ICB-NR and ICB-R tumors. Scale bar, 100 μm (left). Quantification of SQLE fluorescence in the tumor region of ICB-NR ($n = 6$) and ICB-R ($n = 4$) tumors (right). **F**, **G** NADP$^+$/NADPH ratio, ROS (**F**), lipid peroxidation levels (**G**) of shNC or sh*Sqle* cancer cells. **H** Supernatant oxLDL levels of shNC or sh*Sqle* cancer cells cultured with DMEM plus 10% mouse serum for 48 h. **I** Flow cytometry shows Dil-oxLDL uptake in shNC or sh*Sqle* cancer cells ± SSO (100 μM). **J** Schematic of the orthotopic models. **K** Tumor volume of shNC or sh*Sqle* tumors ($n = 6$ mice). **L** Concentration of oxLDL in TIF isolated from shNC or sh*Sqle* tumors ($n = 6$ mice). **M**, **N** Flow cytometry of TREM2, SPP1 expression in TAMs (**M**) and IFNγ expression in tumor-infiltrating CD8$^+$T cells (**N**) ($n = 6$ mice). **O** Schematic of the orthotopic models and treatment. **P** Tumor volume of shNC or sh*Sqle* tumors treated with isotype or anti-PD1 ($n = 6$ mice). **Q**, **R** Flow cytometry of TREM2, SPP1 expression in TAMs (**Q**) and GZMB, IFNγ expression in tumor-infiltrating CD8$^+$T cells (**R**) ($n = 6$ mice). **S** Schematic of experimental treatment in spontaneous HCC model. **T** Tumor burden in mice treated with isotype or anti-PD-1 and Terbinafine or DMSO ($n = 6$ mice). **U**, **V** Flow cytometry of TREM2, SPP1 expression in TAMs (**U**) and GZMB expression in tumor-infiltrating CD8$^+$T cells (**V**) ($n = 6$ mice). Data represent the mean ± SD, $n = 3$ biological replicates in (**F** right), **H**, **I**, $n = 5$ biological replicates in (**F** left), $n = 6$ biological replicates in (**G**). Statistical significance was determined by two-tailed Wald test (**A**), two-tailed Wilcoxon signed rank test (**D**), two-tailed Fisher's exact test (**C** middle), two-tailed unpaired *t* test (**C** right, **E**–**I**, **K**–**N**, **P**–**R**, **T**–**V**), and two-tailed one-sample *t* test (**B**). Schematics in **J**, **O**, and **S** were created in BioRender. Chu, T. (2025) https://BioRender.com/r2v4jgs. Source data is provided as a Source Data file.

discovered that metabolism archetype cancer cells created an immune-inhibitory niche in conjunction with TREM2$^+$TAMs by altering the local TMME profile. While TREM2$^+$TAMs are known to exert an immuno-suppressive role in various types of cancer[14], the mechanisms of their origin and their role in reshaping TME remain elusive in HCC. In this scenario, we uncover that oxLDL is a potential factor driving TREM2$^+$TAM expansion via the TREM2/SYK/CEBPα axis. This is in accord with the recognized role of TREM2 in sensing and uptake of oxLDL by foamy macrophages[50]. Moreover, we show that SPP1, derived from TREM2$^+$TAMs, plays a crucial role in tumor proliferation, invasion, and CD8$^+$T dysfunction. Previous studies have linked SPP1 produced by cancer cells[51], CAF[52], or TAM[53] to malignant progression. Nevertheless, the understanding of molecular mechanisms behind SPP1 production in TAMs was limited. While prior studies proposed hypoxia as a factor to induce SPP1 secretion of TAMs[53], this cannot explain why TAMs formed different subtypes with heterogeneous SPP1 expression, as hypoxia is a common feature of TME in solid tumors[54]. Our results unveiled the significance of oxLDL-mediated TREM2 signaling to control SPP1 secretion of TAMs and HCC progression, providing insights into the differential modulation of TAM phenotype by local TMME.

While abnormal cholesterol metabolism is well-documented in human cancers, its effects on TME have been much less explored. Several studies demonstrated that enriched cholesterol in the TME was responsible for the induction of protumor TAM phenotype[55] and CD8$^+$ T cell exhaustion[56]. A recent investigation reported that tumor-intrinsic X-box binding protein 1 (XBP1) stimulates cholesterol metabolism, which in turn activates MDSCs through the release of small extracellular vesicles[49]. In this study, we pinpointed cancer cell-intrinsic SQLE, a rate-limiting enzyme in cholesterol metabolism, as a potential immunotherapy target due to its significant association with patient survival and immunotherapy resistance in HCC. While the therapeutic potential of targeting SQLE has been demonstrated across various cancer types, prior research has primarily focused on its role in cancer cell proliferation, survival, and evasion[57,58]. Our study broadens the understanding of how tumoral SQLE remodels the TME by facilitating lipid peroxidation and subsequent TREM2$^+$TAM infiltration to diminish anti-tumor immunity. Terbinafine (SQLE inhibitor) is a U.S. Food and Drug Administration–approved oral drug commonly used for the treatment of fungal infections. Previous investigations have demonstrated the satisfying safety profile and relatively few adverse drug–drug interactions of terbinafine[59]. Hence, terbinafine could be a promising immunotherapy adjuvant, and further clinical trials are required to validate the synergistic effect of combining terbinafine and immune checkpoint blockade in HCC treatment.

Although this study identified three functional archetypes of HCC cancer cells, the drivers of these archetypes were not thoroughly explored. We posit that the formation of distinct cancer cell archetypes is primarily attributable to specific genomic alternation characteristics, which requires further investigation. In addition, the HCC neoadjuvant cohort for single-cell sequencing was small. Only scRNA-seq was used in the HCC neoadjuvant cohort, so the number of captured cancer cells was limited. Further studies using combined single-cell/single-nucleus sequencing to demonstrate the evolution of cancer cell heterogeneity in response to therapy will be meaningful.

In summary, our study underscores an oxLDL-mediated interplay between HCC cancer cells of the metabolism archetype and TREM2$^+$TAMs, leading to an immunosuppressive reprogramming of the TME. We show that targeting either TREM2 or SQLE can disrupt this metabolic crosstalk between cancer cells of the metabolism archetype and TREM2$^+$TAMs, thereby reinforcing anti-tumor immunity. Our findings thus shed light on the intricate interplay between HCC cancer cells and TREM2$^+$TAMs in the TME, offering a promising therapeutic avenue for HCC immunotherapies (Supplementary Fig. S12).

Methods

Human samples

This study is approved by the Institutional Review Board (IRB) of Zhongshan Hospital, Fudan University (Reference number: B2021-611). All patients gave informed consent for the collection of clinical information, tissue collection, and research testing.

A total of 33 patients who were pathologically diagnosed with HCC at Zhongshan Hospital, Fudan University, were enrolled in this study. Fresh tumor and adjacent normal tissue samples used for scRNA-seq were collected from 7 treatment-naïve primary HCC patients. Frozen tumor samples used for snRNA-seq and spatial transcriptomics were collected from 16 treatment-naïve HCC patients. Detailed clinical and pathological information, including age, gender (self-reported), and tumor size of these 23 patients, was shown in Supplementary Data 1.

For the establishment of the HCC neoadjuvant cohort, 10 treatment-naïve primary HCC patients at Zhongshan Hospital, Fudan University, were enrolled. These patients received anti-PD1 mAb monotherapy before surgical resection. The collection of fresh tumor samples before the start of immunotherapy, fresh tumor samples after immunotherapy, and fresh adjacent normal tissue samples after immunotherapy was successfully performed in four patients. Formalin-fixed paraffin-embedded (FFPE) tissue blocks of tumor and adjacent normal tissue samples after immunotherapy were obtained from all 10 patients. The clinical responses were assessed according to

modified Response Evaluation Criteria In Solid Tumors (mRICIST) by an independent expert. Based on this criterion, patients with progressive or stable disease were classified as "non-responders", whereas patients with partial or complete response were classified as "responders". Detailed clinical, pathological information, including age, gender (self-reported), tumor size, prognosis, and detailed timeline for neoadjuvant treatment of these 10 patients, was shown in Supplementary Data 2. Most patients underwent surgical resection 3–4 weeks after receiving immunotherapy, except for neoP5 and neoP6, who underwent surgical resection 6–7 weeks after immunotherapy.

Cells

Hepa1-6, HEK-293T, Hep3B, and AML12 cell lines were purchased from ProCell (Wuhan, China). MHCC97H (highly metastatic human HCC cell lines) were established at our institute. Hepa53.4 and Hepalclc7 cell lines were purchased from Zhong Qiao Xin Zhou Biotechnology (Shanghai, China). RIL-175 cell line was purchased from Yaji Biotechnology (Shanghai, China). Cells were cultured at 37 °C in an atmosphere containing 5% CO_2 and in Dulbecco's modified Eagle's medium (Invitrogen) supplemented with 10% fetal bovine serum, unless otherwise stated.

For the culture of AML12 hepatocytes, cells were cultured in DMEM-F12 media (Invitrogen), supplemented with 10% fetal bovine serum, 1% penicillin/streptomycin, 0.5% Insulin-Transferrin-Selenium solution (ProCell, Wuhan, China), and 40 ng/mL Dexamethasone (Sigma).

To generate BMDMs, primary mouse bone marrow cells were flushed from tibias and femurs with ice-cold DMEM and cultured in DMEM supplemented with 10% heat-inactivated FBS, 1% penicillin/streptomycin, and 5 ng/ml mouse macrophage colony-stimulating factor (PeproTech) for 6 days.

To generate human primary macrophages, human peripheral blood mononuclear cells (PBMCs) were first isolated from whole blood obtained from healthy volunteers using SepMate isolation tubes (#85450, Stemcell). Monocytes were then isolated from PBMCs using the EasySep human monocyte isolation kit (#19059, Stemcell) and were differentiated to primary macrophages by culturing with ImmunoCult-SF macrophage medium (#10961, Stemcell) plus 50 ng/mL human macrophage colony-stimulating factor (PeproTech) for 6 days.

Mice

All animal experiment protocols were approved by the Ethics Review Committee of Animal Experimentation at Zhongshan Hospital, Fudan University. Our Ethics Review Committee permitted a maximal tumor size of 20 mm, which was not exceeded in our study. All mice were kept in a controlled, specific pathogen-free environment at room temperature with humidity maintained at 40–60% and a 24-h night-day cycle. All mice received humane care according to the animal welfare guidelines throughout the study. *Trem2*$^{-/-}$ mice were generated by CRISPR Cas9 gene editing from Cyagen Biosciences (Shanghai, China). Male NOD-SCID *Il2rγ*$^{-/-}$ (NSG) mice at the age of 6 weeks were obtained from Cyagen Biosciences. For subcutaneous injections, 6-week-old C57BL/6 or NSG mice were inoculated with hepa1–6 cells with the indicated treatment. The tumor size was measured two times a week using calipers in two dimensions to generate a tumor volume using the formula: $0.5 \times (\text{length} \times \text{width}^2)$. For the establishment of a spontaneous HCC model, 6-week-old wildtype or *Trem2*$^{-/-}$ C57B/L6 mice were injected with 2 ml PBS containing *Ctnnb1*-N90/sg*Tp53* plasmid and sleeping beauty transposon (10 μg per mouse) by hydrodynamic tail vein injection (HDTVi). After 3–4 weeks, mice were euthanized with pentobarbital sodium (40 mg/kg), and the body weight, liver weight, and liver tumor burden were measured. For orthotopic injection, 6-week-old C57BL/6 mice were injected with hepa1–6 cells or mouse spontaneous HCC-derived organoid mixed with or without TREM2$^+$/TREM2$^-$ TAMs or in vitro-induced TAMs with indicated treatment. After 3–4 weeks, mice were euthanized with pentobarbital sodium (40 mg/kg), and the liver tumor size was measured in two dimensions to generate a tumor volume using the formula: $0.5 \times (\text{length} \times \text{width}^2)$. Experiential details are described below.

Mouse hydrodynamic tail vein injection (HDTVi)

Vectors for HDTVi were prepared using the EndoFree Maxi Kit (#12362, QIAGEN) and resuspended in a sterile 0.9% NaCl solution/plasmid mix containing 10 μg of pX330-p53 (Addgene #59910) or pT3-N90-beta-catenin (Addgene #31785), and 10 μg of CMV-SB13 Transposase. CRISPR-Cas9 vector system carrying sgRNAs targeting *Trp53,* together with the Sleeping Beauty Transposon system overexpressing *CTNNB1*-N90 vector in sterile saline, constituted a total volume of 10% of the mouse body weight and were injected into the lateral tail vein of 6-week-old C57BL/6 J mice in 6–8 s as previously described[18,60]. HDTVi-induced tumors were harvested 3–4 weeks after HDTVi.

Subcutaneous, orthotopic, co-injection, and spontaneous HCC model

For the subcutaneous HCC model, 5×10^6 shNC or sh*Sqle* Hepa1-6 cells were implanted into the subcutaneous tissues. For the orthotopic HCC model, 1×10^6 shNC or sh*Sqle* Hepa1–6 cells were resuspended in 20 μl serum-free DMEM medium and injected into the liver of anesthetized 6-week-old male C57BL/6 J mice or male NSG mice. For the co-injection HCC model using Hepa1–6 cells, 1×10^6 Hepa1–6 were 1:1 mixed with isolated TREM2$^+$/TREM2$^-$ TAMs or in vitro-induced TAMs with indicated treatment using serum-free DMEM medium. Eight days before the co-injection experiments, 6-week-old male C57BL/6 J mice were first i.p. injected with Clodronate Liposomes (10 mg/kg; FormuMax) every 2 days for 3 times. The mixed cancer cells and macrophages were then injected into the liver of the anesthetized mice. To establish the HCC spontaneous model, we injected 2 ml PBS containing *CTNNB1*-N90/sg*Trp53* plasmid and sleeping beauty transposon (10 μg per mouse) into mice by HDTVi as described above. For the treatment regime, anti-PD-1 (10 mg/kg for spontaneous HCC model, 5 mg/kg for orthotopic HCC model; BioXCell), anti-SPP1 (10 mg/kg; BioXCell) or mouse IgG2a isotype control (10 mg/kg; BioXCell) was i.p. injected every 3 days, and Terbinafine (80 mg/kg, Targetmol) was i.g. administered every day. All treatments started from day 7 after cancer cell implantation or plasmid injection. At the endpoint, the mice were euthanized with pentobarbital sodium (40 mg/kg), and the tumors were fixed in formalin and embedded in paraffin for IHC and IF analysis or were soaked in tissue preservation solution (Miltenyi Biotec) for flow cytometry analysis.

Generation of organoids and organoid-based orthotopic models

Mouse HCC organoid was isolated from Ctnnb1-N90/sgTrp53 spontaneous HCC tumors using the mouse organoid isolation kit (#abs9552, Absin) according to the manufacturer's protocol. Briefly, fresh tumor tissues were minced into 1–2 mm^2 pieces and enzymatically digested on a heat shaker (37 °C) for 30 min. Then, the digested cell suspension was filtered through a 100 μm filter, followed by treatment with red cell lysis buffer (Thermo Fisher) and resuspended with organoid culture medium. The dissociated cells were then mixed with Matrigel at a ratio of 1:1.5 and seeded onto a 24-well plate. After Matrigel solidified, 500 μL of organoid culture medium was added to the culture plate. The culture medium was replaced every 2 days.

For the generation of organoid-based orthotopic models, mouse HCC organoid was first digested to a single-cell suspension using the digestive solution from the kit. Then, cells were washed with PBS, and 5×10^5 organoid-derived single cells were 1:1 mixed with in vitro-induced TAMs with indicated treatment using PBS. Eight days before

the co-injection experiments, 6-week-old male C57BL/6 J mice were first i.p. injected with Clodronate Liposomes (10 mg/kg; FormuMax) every 2 days for 3 times. The mixed organoid-derived cells and macrophages were then injected into the liver of the anesthetized mice.

Single-cell RNA sequencing

Human and mouse HCC tissues were dissociated for single-cell RNA sequencing using the human tumor dissociation kit (130-095-929, Miltenyi Biotec) and the mouse tumor dissociation kit (130-096-730, Miltenyi Biotec), according to the manufacturer's protocol. Briefly, the tissue was placed in a petri dish on ice and cut into small pieces of 2–4 mm. The pieces were infused with the RPMI/enzyme mix (Miltenyi Biotec), transferred to a gentleMACS C tube containing RPMI/enzyme mix, attached to the sleeve of the gentleMACS Octo Dissociator, and run the program. After termination of the program, the suspension was passed through a 70 μm strainer and spun down at 300×*g* for 10 min at 4 °C, resuspended in PBS containing 0.04% BSA. Red blood cells were lysed with red blood cell lysis solution (130-094-183, Miltenyi Biotec) at 4 °C for 10 min, the resulting suspension was centrifuged at 300×*g* for 10 min and resuspended in PBS containing 0.04% BSA. Viability was assessed to be >85% using CountStar. Viability enrichment was performed using the Dead Cell Removal Kit (130-090-101, Miltenyi Biotec), according to the manufacturer's protocol. Dissociated cells were resuspended in a final solution of PBS containing 0.04% BSA prior to loading on the 10× Chromium platform. The scRNA-seq libraries were generated using the 10× Genomics Chromium Controller Instrument and Chromium Single Cell 3′ V3 Reagent Kits (10× Genomics, Pleasanton, CA), according to the manufacturer's recommendations. The experiments were performed by Berry Genomics Corporation (Beijing, China).

Single-nucleus RNA sequencing

To isolate single nuclei from human HCC samples, tissues were dissected and placed in 2 mL PBC medium in a 5 mL tube on ice. The PBC medium was removed to a 15 mL conical and kept on ice. Two microliters of chilled lysis buffer (10 mM Tris-HCl, 10 mM NaCl, 3 mM $MgCl_2$, and 0.1% Nonidet™ P40 Substitute in Nuclease-Free Water) were added to the tissue, and the tissues were homogenized 10 times through a tissue grinder. After homogenization, the tissue was lysed on ice for 15 min, swirling 2–3 times during this incubation period. The reserved chilled HEB media was then returned to the lysed tissue solution, and the tissue was further triturated with 5–7 passes through a 1 mL pipette. A 30 μm cell strainer (130-110-915, Miltenyi Biotec) was washed with 1 mL of PBS, and the lysed tissue solution was filtered through the strainer to remove debris and clumps. Filtered nuclei were centrifuged at 500×*g* for 5 min at 4 °C. The supernatant was removed, and nuclei were washed in 1 mL of Nuclei Wash and Resuspension Buffer (1× PBS with 1.0% BSA and 0.2 U/μl RNase Inhibitor). Nuclei were manually counted by Trypan blue and AO-PI after each centrifugation (400×*g*, 10 min, 4 °C) and resuspended. Single nuclei were processed using Chromium Controller (10× Genomics), according to the manufacturer's protocol. The experiments were performed by Shanghai Biochip Corporation (Shanghai, China).

Spatial transcriptomic sequencing

Human HCC tissues were embedded in OCT. The RNA quality of the OCT OCT-embedded tissue block was assessed by calculating the RNA Integrity Number (RIN) of RNA extracted from tissue sections. Only tissue blocks with RIN ≥ 4 were used for spatial transcriptomic sequencing. The tissues were sectioned into 10 μm sections. The sections were fixed with chilled Meathol at −20 °C and proceeded to H&E Staining. Sections were then imaged, destained, and transferred to a Visium CytAssist Spatial Gene Expression slide. The probe extension and library construction steps follow the standard Visium CytAssist Spatial Gene Expression workflow outside of the instrument. Libraries were sequenced on the Illumina NovaSeq6000 platform with PE150 mode. The experiments were performed by Berry Genomics Corporation (Beijing, China).

Flow cytometry

For flow cytometry analysis of mouse HCC tumors, tumor tissues were digested at 37 °C for 30 min with 1 mg/ml Collagenase D and 0.1 mg/ml DNase I (Roche). Digestion was stopped by EDTA, and cells were filtered through 70 mm cell strainers and washed twice with PBS containing 1 mM EDTA and 2% FBS (staining buffer). Cells were resuspended in the staining buffer and first stained with mouse TruStain FcX (Biolegend, 1:200) on ice for 10 min. Then, cells were stained with the following antibodies on ice for 30 min: CD45 (Clone 30-F11, Biolegend, 1:200), CD3 (Clone 145-2C11, Biolegend, 1:200), CD8 (Clone 53-6.7, Biolegend, 1:200), CD11b (Clone M1/70, Biolegend, 1:200), F4/80 (Clone BM8, Biolegend, 1:200) and TREM2 (Clone #237920, R&D Systems, 1:200). For intracellular staining, cells were fixed with fixation buffer (Biolegend) on ice for 15 min, and then washed twice with Intracellular Staining Permeabilization Wash Buffer (Biolegend). Antibodies against IFNγ (Clone XMG1.2, Biolegend, 1:200), Granzyme B (Clone QA16A02, Biolegend, 1:200), and SPP1 (#IC808P, R&D Systems, 1:200) were added and incubated for 1 h on ice. Cells were resuspended in the staining buffer again and then analyzed on Fortessa (BD Biosciences). The flow cytometry data were analyzed by FlowJo v10 (BD Biosciences).

For flow cytometry analysis of human HCC tumors, fresh tumor tissues were digested, and single-cell suspension was prepared as described above. Cells were stained with human TruStain FcX (Biolegend, 1:200) and then stained with the following antibodies: CD45 (Clone HI30, BioLegend, 1:200), CD11b (Clone M1/70, BD Biosciences, 1:200), CD14 (Clone MφP9, BD Biosciences, 1:200), TREM2 (Clone #237920, R&D Systems, 1:200) and SPP1 (Clone 2F10, Invitrogen, 1:200). All surface staining, intracellular staining and data analysis were performed as described above.

For flow cytometry analysis of in vitro cultured cells, human or mouse macrophages or $CD8^+$T cells with indicated treatment were harvested and washed twice with the staining buffer. Macrophages were first stained with human or mouse TruStain FcX (Biolegend, 1:200) before incubating with the primary antibodies. The following antibodies were used for staining of in vitro cultured cells: anti-human/mouse TREM2 (Clone #237920, R&D Systems, 1:200), anti-mouse SPP1 (#IC808P, R&D Systems, 1:200), anti-human SPP1 (Clone 2F10, Invitrogen, 1:200), anti-mouse IFNγ (Clone XMG1.2, Biolegend, 1:200), anti-human IFNγ (Clone 25723.11, BD Biosciences, 1:200) and anti-human/mouse phospho-SYK (Clone F.724.5, Invitrogen, 1:200). All surface staining, intracellular staining and data analysis were performed as described above. Gating strategies for in vitro and in vivo flow cytometry experiments were reported in Supplementary Fig. S13.

Isolation of primary macrophages

Human and mouse HCC tumors were digested, and single-cell suspensions were prepared as described above. After being filtered through 70 mm cell strainers, red cell lysis was performed, and single cell suspensions were stained with the indicated antibodies in staining buffer. The following antibodies were used to isolate $TREM2^+$ or $TREM2^-$ TAMs from human HCC tissues: CD45 (Clone HI30, BioLegend, 1:200), CD11b (Clone M1/70, BD Bioscience, 1:200), TREM2 (Clone #237920, R&D Systems, 1:200). The following antibodies were used to isolate $TREM2^+$ or $TREM2^-$ TAMs from mouse HCC tissues: CD45 (Clone 30-F11, Biolegend, 1:200), CD11b (Clone M1/70, Biolegend, 1:200), F4/80 (Clone BM8, Biolegend, 1:200), TREM2 (Clone #237920, R&D Systems, 1:200). Staining with antibodies was performed for 30 min on ice. Human $TREM2^+$TAMs ($CD45^+CD11b^+TREM2^+$), human $TREM2^-$TAMs ($CD45^+CD11b^+TREM2^-$), mouse $TREM2^+$TAMs ($CD45^+CD11b^+F4/80^+TREM2^+$), and mouse

TREM2⁻TAMs (CD45⁺CD11b⁺F4/80⁺TREM2⁻) were acquired by flow cytometric cell sorting (BD FACS AriaIII). Isolated TAMs were cultured in 10% FBS DMEM, and the culture medium was changed once a day. Gating strategies for TREM2⁺/TREM2⁻ TAM identification were reported in Supplementary Fig. S13.

Tumor conditioned medium collection and in vitro induction of TAMs

To collect tumor conditioned medium, after reaching 80% confluence in 75 cm^2 BD Falcon flasks, cancer cells were passed into 3 new 75 cm^2 flasks with fresh DMEM supplemented with 10% heat-inactivated FBS and 1% penicillin/streptomycin. Supernatants were collected after 48 h. The conditioned medium was transferred to a 15-ml Falcon tube and centrifuged at 250×*g* for 8 min. The supernatant was sterile-filtered using a 0.22-mm filter (Millex-GP) with a 10-ml syringe barrel.

To generate in vitro-induced TAMs, BMDMs were cultured with freshly collected tumor-conditioned medium mixed with 10% FBS DMEM medium at a ratio of 1:1, and cells were cultured for 48 to 72 h before further functional analysis or in vivo co-injection experiments.

Generation of stable cells with *Sqle* depletion

To deplete Sqle in Hep1–6 cells, 3 mg PLKO.1 plasmid of shNC or sh*Sqle* (Sigma), 1 mg pCMV packaging vector, and 1.5 mg PVSV-G enveloped vector were co-transfected into HEK293T cells in 60 mm cell culture dishes (NEST). After 48 and 72 h, virus-containing supernatant was collected and filtered through a 0.45 mm PES Syringe Filter (Sigma), and then was used to infect cancer cells in the presence of 8 mg/ml Polybrene (Sigma). Afterward, 4 μg/ml puromycin (Beyotime) was added to select the positive infected cells for 5 days, and stable cell lines were further maintained under puromycin.

Generation of macrophages with *Cebpa* depletion

Lentivirus-induced *Cebpa* knockdown was conducted in BMDMs according to previously described protocols[61]. Briefly, a virus containing the shNC or sh*Cebpa* plasmid was prepared as described above. Bone marrow cells were isolated and cultured with differentiation medium for 3 days, as described above. At day 4, 50 M.O.I. of virus was used to infect bone marrow cells in the presence of 6 mg/ml Polybrene (Sigma). The bone marrow cells were incubated with the virus for 48 h. Then, the virus-containing medium was replaced by differentiation medium to allow for the completion of the differentiation process at day 7. The transduction efficiency was estimated by analyzing the mRNA and protein levels of target genes. The shRNA sequences used in this study were listed in Supplementary Table 1.

Cell viability and proliferation analysis

Cell viability was determined using the 3D CellTiter-Glo (G9681, Promega) kit, according to the manufacturer's protocol, by adding 80 μl of CellTiter-Glo 3D Reagent to each well of the 96-well plate. The plate was incubated at room temperature for 30 min before recording the luminescence using the plate reader.

Conditioned medium from in vitro-induced or isolated TAMs with indicated treatment was obtained by culturing cells for 24 h. Then, 1×10^4 cancer cells were seeded on the 96-well plate and cultured with the indicated conditioned medium. Cell proliferation analysis was performed with Cell Counting Kit 8 (C0037, Beyotime), according to the manufacturer's protocol.

Western blot

The antibodies used for western blotting were purchased commercially, including β-tubulin (#2128, Cell Signaling Technology), GAPDH (60004-1-Ig, Proteintech), CEBPA (#8178, Cell Signaling Technology), SYK (PA5788, Abmart), phospho-SYK (TA3314, Abmart), DNMT3A (#49768, Cell Signaling Technology), CD36 (T55796, Abmart), or SQLE (PA5-54265, Thermo Fisher Scientific).

Intracellular proteins of cells or tumor tissues were extracted using RIPA lysis buffer (Beyotime) plus protease inhibitor cocktail (MCE) on ice. The collected protein samples were subjected to sodium dodecyl sulfate-polyacrylamide gel electrophoresis (SDS-PAGE) and transferred onto PVDF membranes (Millipore). Subsequently, membranes were blocked for 1 h with nonfat dry milk solution (5% in TBS) containing 0.1% Tween-20. The blots were subsequently probed with the indicated primary antibodies and the corresponding secondary antibodies. Immunoreactive bands were visualized by enhanced chemiluminescence (Millipore).

Quantitative real-time PCR (qPCR)

Total RNA from cells was extracted using TRIzol reagent, and cDNA was synthesized using EasyScript One Step gDNA Removal and cDNA Synthesis SuperMix (TransGen). Quantitative PCR was performed using TransStart Top Green qPCR SuperMix (TransGen) on the StepOnePlus system (ABI). The qPCR conditions were 94 °C for 30 s, followed by 40 cycles of 94 °C for 5 s and 60 °C for 31 s. Amplification of specific transcripts was confirmed by melting curve profiles generated at the end of the PCR program. Expression levels of target genes were normalized to the expression of the *Actb* or *GAPDH* gene and were calculated based on the comparative cycle threshold method ($2^{-\Delta\Delta Ct}$). Specific primers for qPCR were listed in Supplementary Table 1.

Isolation and activation of CD8⁺ T cells

Mouse CD8⁺T cells were isolated from the spleens of C57/BL6 mice using the EasySep mouse CD8⁺T cell isolation kit (#19853, Stemcell). Human CD8⁺T cells were isolated from fresh peripheral blood mononuclear cells obtained from healthy donors using the EasySep human CD8⁺T cell isolation kit (#17953, Stemcell). For CD8⁺T cell activation, 1 mg/ml anti-human/mouse CD3 and anti-human/mouse CD28 (Biolegend) were coated to the culture dish and incubated at 4 °C overnight. Then, purified CD8⁺T cells were added to the antibody-coated culture dish and cultured with RPMI 1640 containing 50 U/mL IL-2 (PeproTech), 10% FBS, 10 mM HEPES, 100 mM NEAA, and 50 mM β-Mercaptoethanol (Gibco) for 24 h.

Co-culture experiments

Co-culture experiments were performed by seeding in vitro-induced or in vivo-isolated TAMs with indicated treatment in the lower chamber and cancer cells or activated CD8⁺T cells in the upper chamber of a 6-well or 24-well transwell apparatus with 0.4 μm pore size (Corning Incorporated).

Isolation of primary cancer cells from mouse HCC tumors

The isolation of primary cancer cells in TREM2⁺TAM/TREM2⁻TAM co-injection tumors was performed with a cancer cell isolation kit (130-110-187, Miltenyi Biotec). Briefly, the resected tumors were dissociated with the tumor dissociation kit (Miltenyi Biotec) as described above. Then, primary cancer cells were negatively selected by magnetic separation. The purity of the obtained cancer cells was determined by flow cytometry analysis of AFP expression (an HCC cancer cell marker).

Transwell migration and invasion assay

The 24-well transwell chamber with 8 μm pore size (Corning Incorporated) was employed for migration and invasion assay. Briefly, cancer cells were allowed to reach 80% confluence and starved for 24 h. The cells were then resuspended in serum-free DMEM and diluted to 2×10^5/mL. The upper chamber was added with 100 μL cancer cells, and the lower chamber was added with 600 μL DMEM containing 10% serum. The lower chamber also contains pre-seeded TAMs with indicated treatment. The cells were cultured for 48 h, and the cells in the upper chamber were cleaned. After that, the chamber was rinsed with PBS and immersed in precooled 4% paraformaldehyde for 30 min. Cells transferred to the lower chamber were fixed and stained with

0.1% crystal violet (Biosharp) for 10 min. Five random fields were selected, and the migrated cells were counted using ImageJ software. The cell invasion assay was carried out using Matrigel (Corning Incorporated). The Matrigel was melted at 4 °C and then diluted with serum-free DMEM at a ratio of 1:8. Other operations were the same as the cell-migration procedures.

Immunofluorescence staining

The antibodies used for immunostaining and IHC were purchased commercially, including SPP1 (ab214050, Abcam, 1:1500), TREM2 (MAB17291, R&D Systems, 1:1500), Ki-67 (ab15580, Abcam, 1:2000), CD68 (ab955, Abcam, 1:3000), SQLE (PA5-54265, Thermo Fisher Scientific, 1:500), F4/80 (ab300421, Abcam, 1:5000), oxLDL (ab14519, Abcam, 1:1000), APOE(#13366, Cell Signaling Technology, 1:1000), CD44 (ab189524, Abcam, 1:4000) and SAA1 + SAA2 (ab207445, Abcam, 1:1000).

Tissue paraffin embedding was performed using a standard protocol. Paraffin-embedded tissues were cut into 7 mm sections and stored at room temperature. Frozen tissues were cut into 8 mm sections and stored in a −30 °C freezer before staining. Sections were then blocked with 5% goat serum (ZSGB BIO) for 1 h and incubated with primary antibodies at 4 °C overnight in the dark. The slides were washed 3 times with PBS. 1 mg/ml DAPI (Life Technology) was added and incubated for 5 min. After a final wash step, sections were mounted using the Fluoromount-G (SouthernBiotech 0100-01). Immunofluorescence was visualized utilizing a confocal microscope (ZEISS LSM880).

ELISA

The concentration of SPP1 in cell culture supernatant was determined with the mouse SPP1 ELISA kit (U96-1583E, Yobibio) or human SPP1 ELISA kit (U96-1582E, Yobibio). The oxLDL levels in mouse TIF and serum were determined with a mouse oxLDL ELISA kit (U96-3617E, Yobibio). The oxLDL, VLDL, HDL, and LDL levels in human TIF and serum were determined with a human oxLDL ELISA kit (JL12154, Jianglai), a human VLDL ELISA kit (JL14806, Jianglai), a human HDL ELISA kit (JL10023, Jianglai), and a human LDL ELISA kit (JL10816, Jianglai). All ELISA experimental procedures were performed according to the manufacturer's instructions.

Lipid treatment of TAMs

To investigate the effect of different types of lipids on TREM2 and SPP1 expressions in TAMs, we performed in vitro induction of TAMs as described above. The TAMs were then treated with the following lipids for 48 h: Palmitic acid (100 μM, MCE), Stearic acid (90 μM, MCE), Palmitoleic acid (100 μM, MCE), Oleic acid (100 μM, MCE), Cholesterol esters (Cholesteryl behenate, 10 μg/mL, MCE), Cholesterol (10 μg/mL, MCE), Ceramides mixture (20 μg/mL, MCE), L-carnitine (60 μg/mL, MCE), oxLDL (50 μg/mL, Invitrogen), LDL (50 μg/mL, Invitrogen) and HDL (50 μg/mL, Invitrogen). After the lipid challenge, TAMs were harvested, and the TREM2 and SPP1 expressions were analyzed by flow cytometry. Culture supernatants were also collected for the measurement of SPP1 concentration by ELISA.

Isolation of tumor interstitial fluid and plasma

The isolation of tumor interstitial fluid (TIF) and plasma was performed as described previously[62]. Briefly, fresh human or mouse HCC tumor tissues were harvested, rinsed with 1× PBS, and blotted on filter paper (VWR, 28298-020) to remove the surface liquid. Then, the tumors were put onto 20 μm nylon filters (Millipore) affixed atop 50 mL tubes, and centrifuged for 10 min at 4 °C, 106×*g*. The TIF was then collected from the conical tube, frozen in liquid nitrogen, and stored at −80 °C until further analysis. For culturing cells with TIF, the TIF was filtered through a 0.22 μm filter (Millex-GP) and mixed with 10% FBS DMEM medium at a ratio of 1:10. For isolation of plasma, human or mouse blood was first centrifuged for 10 min at 4 °C, 845×*g* to separate plasma. The isolated plasma was frozen in liquid nitrogen and stored at −80 °C until further analysis.

Removal of lipids and lactic acid in tumor interstitial fluid

For the removal of lipids in tumor interstitial fluid, we used the Cleanascite Lipid Removal Reagent (#X2555-10, Biotech Support Group), according to the manufacturer's protocol. Briefly, the tumor interstitial fluid was mixed with Cleanascite Lipid Removal Reagent at a ratio of 2:1 by gently shaking periodically for 10 min. Then, the mixture was centrifuged at 16,000×*g* for 1 min, and the supernatant was decanted into new tubes for downstream analysis.

For the removal of lactic acid in tumor interstitial fluid, we used 0.5 M Na_2CO_3 solution (#S885117, Macklin, Shanghai, China) to neutralize lactic acid. PANPEHA Whatman paper (Sigma) was used to confirm pH 7.0-7.5 after neutralization.

Examination of oxLDL production by cultured cells

For the examination of oxLDL production by cultured cells, the fetal bovine serum in the culture medium was replaced with mouse serum (#abs937, Absin) or human serum (#H6914, Sigma) to avoid the induction of different-species lipoproteins, while the other components remained unchanged. Briefly, 1×10^5 cells were seeded onto a 24-well plate and cultured for 48 h. Then, the supernatant was collected, centrifuged at 250×*g* for 5 min, and used for oxLDL ELISA measurement.

Chromatin immunoprecipitation-qPCR (ChIP-qPCR) assays

The ChIP-qPCR assays were performed using the ChIP kit (#53040, Active Motif). The procedure was according to the kit instruction manual provided by the manufacturer. Briefly, 1×10^7 BMDMs with indicated treatment were fixed by 1% formaldehyde, fragmented by sonication to shear the chromatin to 200–1000 bp. The sheared crosslinked chromatin was incubated with IgG and anti-CEBPα (#8178, Cell Signaling Technology) overnight, followed by Protein A/G conjugated agarose beads incubation. The precipitated DNA was amplified by primers and quantified by the StepOnePlus system (ABI). ChIP primer sequences were listed in Supplementary Table 1.

Immunoprecipitation (IP) assays

For IP assays, cells were lysed and washed in RIPA lysis buffer (Beyotime) supplemented with protease inhibitor cocktail (MCE). Cell lysates were incubated overnight at 4 °C with the indicated primary antibody and protein A/G agarose beads (MCE). Beads were centrifuged at 1000×*g* for 5 min at 4 °C to remove the supernatant, washed 4 times with the IP buffer, and boiled in SDS-loading buffer for 5 min at 95 °C. Samples were then analyzed by Western blot as described above.

Generation and viability assessment of patient-derived organoids

The generation of patient-derived organoids was performed using the human liver cancer organoid kit (KOG02-HC, Orgenbiotech) according to the manufacturer's protocol. Briefly, fresh HCC samples were minced into 1–2 mm^2 pieces and digested on a heat shaker (37 °C) for 1 h. Then, the digested cell suspension was filtered through a 100 μm filter, followed by treatment with red cell lysis buffer, and resuspended with organoid culture medium. The dissociated cells were then mixed with Matrigel at a ratio of 1:1.5 and seeded onto a 24-well plate. After Matrigel solidified, 500 μL of organoid culture medium was added to the culture plate. The culture medium was replaced every 2 days.

For the viability assessment of HCC organoids, cells were first seeded onto a 24-well plate and incubated for 24 h in organoid culture

medium with Matrigel. Then, TNF (100 ng/mL) + IFNγ (100 ng/mL) (TNF/IFNγ), TNF/IFNγ plus SPP1 (50 ng/mL) or a combination of TNF/IFNγ, SPP1, and integrin inhibitor TFA (HY-100445A, MCE, 50 μM) was added to the culture medium. Organoids were treated for 12 days in total with inhibitors/cytokines refreshed every 4 days. On day 12, viability assessment was performed using the 3D CellTiter-Glo (G9681, Promega) kit according to the manufacturer's protocol.

DNA extraction and bisulfite (BS)-PCR

Briefly, 500 ng of genomic DNA was extracted from the indicated cells using a commercial DNA extraction kit (#69504, QIAGEN). The extracted DNA was then Bisulfite converted using DNA Bisulfite Conversion Kit (#D0068S, Beyotime) and PCR amplified. The target DNA products were inserted into a T vector, and 10 clones from each sample were randomly picked for sequencing. Primer sequences are listed in Supplementary Table 1.

DNMT activity analysis

DNMT activity in the nuclear extracts was quantified using an EpiQuik DNMT Activity/Inhibition Assay Ultra Kit (#P-3009-48, Epigentek), following the instructions of the manufacturer.

SiRNA and transfection

The siRNA sequences were designed by Genecfps (Jiangsu, China). All siRNA sequences were listed in Supplementary Table 1. For siRNA transfection, cells were transfected with siRNA (10 μM) using Advanced DNA RNA Transfection Reagent (Zeta Life) according to the manufacturer's instructions.

Liquid chromatography–mass spectrometry (LC–MS) analysis

The 5mC levels of genomic DNA were determined by LC–MS analysis. The Quantification of 5mC DNA contents was performed by MetWare (Shanghai, China) based on the AB Sciex QTRAP 6500 LC–MS/MS platform.

Dual-Luciferase reporter assay

Wild-type and mutant 3′UTR sequences of *Trem2* and *Spp1* were synthesized and inserted into the pGL3 promoter vector by Genomeditech (Shanghai, China). Cells were co-transfected with the 3′-UTR wildtype or mutant plasmid and *Cebpa* overexpression or negative control plasmid using Lipofectamine 3000 (Invitrogen). Forty-eight hours post-transfection, relative luciferase activity was measured using the Dual-Luciferase® Reporter Assay System (Promega) according to the manufacturer's instructions. Firefly luciferase activity was normalized to Renilla luciferase activity.

Measurement of lipid peroxidation, $NADP^+$/NADPH ratio, and ROS

The lipid peroxidation levels were determined using Image-iT Lipid Peroxidation Kit (#C10445, Invitrogen) according to the manufacturer's protocol. Briefly, 10 μM of Image-iT Lipid Peroxidation Sensor was added to cultured cells and incubated for 30 min at 37 °C. Then, the fluorescence at 581/591 nm (reduced dye) and 488/510 nm (oxidized dye) was measured with a SpectraMax M3 microplate reader (Molecular Devices). The NADP+/NADPH ratio was measured using the NADP+/NADPH Assay Kit with WST-8 (#S0179, Beyotime) according to the manufacturer's protocol. Intracellular ROS was measured using the ROS Assay Kit (#S0033S, Beyotime) according to the manufacturer's protocol. The ROS levels were normalized with total protein levels measured by the BCA assay (#P0010S, Beyotime).

Alignment and quantification of single-cell and single-nucleus data

For single-cell and single-nucleus data, the raw reads were mapped to the human reference genome (refdata-gex-GRCh38-2020-A) or mouse reference genome (refdata-gex-mm10-2020-A) using CellRanger count (v6.0.0, 10× Genomics) with default parameters. The "raw_feature_bc_matrix.h5" file outputted by the CellRanger count pipeline was used for downstream background noise removal.

Removal of background noise in gene expression matrices

We used the remove-background function of CellBender v0.2.0 to remove ambient-RNA and empty droplets from raw gene expression matrices[63]. The parameter "expected-cells" was estimated by CellRanger, and the parameter "total-droplets-included" was set to a value between 15,000–50,000, representing a point within the plateau of the barcode rank plot. All other training parameters were set to default.

Quality control and filtering

The "output_filtered.h5" file produced by CellBender was used for quality control and filtering. We excluded genes expressed by fewer than 10 cells and excluded cells expressing fewer than 400 genes or more than 10% mitochondrial content (20% content in mouse). We also detected potential doublets using Scrublet and DoubletFinder on a per-library basis. The predicted doublets were filtered from the datasets. After the above quality control process, we only kept the protein-coding genes for downstream analysis, as described previously[64].

Integration of single-cell data across different batches

For the integration of human single-cell and single-nucleus sequencing data, i.e., single-cell data across different sequencing techniques, we utilized scANVI[21] for data integration according to their recommended practices. Briefly, the scRNA-seq data and snRNA-seq data were merged and normalized using the log-normalization method (Scanpy v1.8.3). We identified highly variable genes ($n = 2000$) using Seurat v3 flavor on the raw counts, which were used to train the initial integration model using single-cell variational inference (scVI) v.0.6.8. We corrected for sequencing technique, sample source, and origin of the data in the scVI integration process. Then, we initialized the scANVI model based on the pre-trained scVI model, using pre-assigned cell labels to get more accurate integration. The pre-assigned cell labels were obtained by analyzing single-cell and single-nucleus data separately using the workflow described below. The resulting latent representation of each cell was used for clustering, cell type annotation, and uniform manifold approximation and projection (UMAP) visualization.

For the integration of human or mouse single-cell data from the same sequencing technique, we used the Harmony algorithm[65] for batch correction. Briefly, the scRNA-seq or snRNA-seq data were log-normalized, subset to 2000 highly variable genes, and scaled using Seurat v4.0.3. Then, principal component analysis (PCA) was performed, and the top 50 principal components were used as input for Harmony, which removed the bias resulting from sample source and data set origin. Subsequently, the top 30 Harmony dimensions were selected for clustering, cell type annotation, and UMAP visualization.

Clustering and annotation of cell types

We used the Leiden clustering method (Scanpy v1.8.3) to find different cell clusters based on the latent representation obtained from scANVI or Harmony integration. The resolution parameter was set to 1.2 for major cell type identification and 0.8 for subtype characterization of major cell types. For cell type annotation, the main cell types were identified by manual annotation of differentially expressed genes between clusters based on known markers and signatures[66]. The initial labeling identified endothelial, hepatocytes, stromal, granulocytes, monocyte/macrophages, proliferating, T, NK, B, and plasma cell populations. Next, we split the data into subsets of the main labels and reran scaling, PCA, UMAP dimension reduction, clustering, and DE analysis on each subset

as described above. The resulting clusters were manually annotated and used as cell subtype labels for each major cell population.

Tissue enrichment of cell types

To quantify the enrichment of cell clusters across tissue types, we calculated the odds ratio (OR) to indicate tissue preference as described previously[67]. Briefly, for each combination of cell cluster i and tissue j, a 2 by 2 contingency table was constructed, which contained the number of cells of cluster i in tissue j, the number of cells of cluster i in other tissues, the number of cells of non-i clusters in tissue j, the number of cells of non-i clusters in other tissues. Then Fisher's exact test was applied to this contingency table, thus OR and the corresponding *p*-value could be obtained. *P*-values were adjusted using the "BH method" implemented in the R function p.adjust. Consistent with previous observation[67], we found that all ORs > 1.5 or ORs < 0.5 had adjusted *p*-values < 1e−10. Hence, a higher OR with a value > 1.5 indicated that cell cluster i was more preferred to distribute in tissue j, and a lower OR with a value < 0.5 indicated that cell cluster i was preferred not to distribute in tissue j.

Non-negative matrix factorization

For cancer cells in each snRNA-seq sample, we applied non-negative matrix factorization (R NMF package, v0.26, with algorithm set to "nndsvd" and number of factors set to 10) to the scaled and centered expression data (Seurat SCTransform function), after converting all negative values to zero. The selection of factor number 10 was based on previously published studies[68–70]. For each of the resulting 10 factors, 50 genes with the highest NMF scores were defined as a signature. To identify coherent expression programs across cancer cells of different samples, we aggregated 120 signatures from 12 samples and did hierarchical clustering using the Pearson correlation coefficient. This revealed the 8 metaprograms described in this study. Then, for each metaprogram, we calculated the expression score using genes in the metaprogram and ranked all the genes by their correlation with the expression score. Each meta-program was redefined using the top 50 correlated genes. The top 50 genes for obtained human snRNA-seq meta-programs were listed in Supplementary Data 3. To infer the co-occurrence of metaprograms, Pearson correlation coefficients were calculated between the signature scores of NMF programs of all malignant hepatocytes in snRNA-seq data. After the determination of NMF metaprograms, i.e., cancer cell functional archetypes, we assigned each cancer cell in snRNA-seq data to one of these archetypes based on the metaprogram that has the maximum NMF coefficient in this cell. The same procedure was performed on human scRNA-seq data and mouse scRNA-seq data, and the top 50 genes for corresponding meta-programs were listed in Supplementary Data 3.

Annotation of NMF metaprograms and cancer cell archetypes

The annotation of the obtained NMF metaprograms was performed based on the top 50 genes ranked by NMF scores. Metaprogram P1 was classified as a lipoprotein metabolism program, characterized by genes of apolipoprotein (e.g., *APOC1*, *APOE*, *CLU*). Metaprogram P2 was enriched for genes associated with xenobiotic metabolism (e.g., *ABCB11*, *ACSM2B*, *CYP2A7*). Metaprogram P3 was annotated as lipid metabolism programs, encompassing genes of fatty acid metabolism (e.g., *MFSD2A*, *PLIN5*, *PPARA*) and cholesterol metabolism (e.g., *FDPS*, *HMGCS1*, *SQLE*). Metaprogram P4 was enriched by markers of DNA replication (e.g., *DTL*, *RRM2*) and G2/M phases (e.g., *ASPM, CENPE, TOP2A*), and was classified as a proliferation program. Metaprogram P5 represented acute-phase response, such as (e.g., *A2M, CRP, SAA1*), and was enriched for complement regulation markers (e.g., *C5, CFH, CFHR3*). Metaprogram P6 encompassed epithelial-to-mesenchymal transition (EMT) genes (e.g., *AKT3, ANXA4, FYN*). Metaprogram P7 was characterized by protein folding (e.g., *HSP90AB1, HSPD1, TRAP1*) and translation markers (e.g., *BOP1, EIF3A, EIF3B*). The final metaprogram P8 was defined by cancer stemness-related genes (e.g., *CD44, BIRC3, SOX4*).

The determination of functional archetypes was performed via the calculation of Pearson's correlation between NMF metaprograms. P1 (lipoprotein metabolism) was positively correlated with P2 (xenobiotic metabolism) and P3 (cholesterol/fatty acid metabolism), while it followed a strong co-exclusion pattern with P6 (EMT), P7 (protein folding/translation), and P8 (cancer stemness). Furthermore, there was a significant correlation between P6, P7, and P8, and concomitant mutual exclusivity with P1, P2, and P3. Additionally, P4 (acute phase/complement response) was negatively correlated with P1/P2/P3 and P6/P7/P8. Therefore, this correlation analysis revealed that there are three single-cell archetypes that co-existed in HCC cancer cells: one high in lipoprotein, xenobiotic and cholesterol/fatty acid metabolism (P1, P2, P3), denoted as metabolism archetype; one high in acute-phase response and complement regulation, denoted as inflammation archetype; and the other high in EMT, protein folding/translation and cancer stemness program, denoted as stemness archetype.

Among the identified top genes of NMF metaprograms, APOE was reported as a key gene involved in the lipid transport and metabolism function of cancer cells[71]; SAA1/2 is an acute-phase response protein that was primarily derived from hepatocytes and upregulated during hepatic inflammation[72]; and CD44 is a well-established cancer stem cell (CSC) marker that was validated in multiple cancer types[73]. We therefore chose APOE, SAA1/2, and CD44 as markers of metabolism, inflammation, and stemness archetype cancer cells to validate their spatial co-exclusion pattern at the protein level, since they were representative of the lipid metabolism, acute-phase response, and stemness features that correspond to the metabolism, inflammation, and stemness archetype cancer cells.

Cross-species comparison of cell types using Support Vector Machine

To compare the transcriptional signatures of cell types in human single-cell data with their mouse counterparts, we trained a Support Vector Machine (SVM) classifier on the human single-cell dataset and projected the cell type annotations onto the mouse scRNA-seq data as previously described[74]. The SVM-predicted annotations were compared to the manual annotations of cell clusters based on marker genes. Briefly, human data sets were first downsampled to the clusters with the lowest cell number to obtain a balanced dataset. Seventy-five percent of the data was used for model training, and 25% of the data was used for model testing. Raw expression matrices were log-normalized and subset to the 300 most highly variable genes, which were used as features for model training. Then, we trained an SVM classifier on the human training data using sklearn v1.2.2, with kernel set to "rbf", gamma set to 0.001, and probability set to True, which enables probability estimates by 5-fold cross validation. The performance of the model was checked based on the precision, recall, and F1-score per cell type label. After that, the gene identifiers in mouse scRNA-seq data were converted to human genes using the biomaRt R package v2.56.0. The trained model was then used to project the human cell type labels onto the gene-harmonized mouse datasets. The SVM-predicted probability of each cell in the mouse datasets corresponding to every given human cell type was obtained. The estimated probabilities between human and mouse matching cell types were summarized and used as a similarity score.

SCENIC analysis

We utilized SCENIC v0.12.1 to predict transcription factor (TF) activities in single-cell data. Briefly, co-expression modules between TFs

and target genes were inferred using GRNBoost based on correlations between the expression of genes across snRNA-seq-derived cancer cells. RcisTarget then refined the selection of modules by keeping only modules with a significantly enriched TF binding motif. Subsequently, AUCell scored the activity of each regulon in each cell.

Copy number variation analysis

For each snRNA-seq sample and neoadjuvant cohort sample in our dataset, we used the inferCNV algorithm (infercnvpy v0.4.0) to infer the copy number variation (CNV) of each hepatocyte-linage cell, using the average patterns of non-tumor immune cells as a reference for the CNV estimation. Malignant hepatocytes were further distinguished from non-malignant hepatocytes by the large-scale CNVs of each cell as described previously[69].

Differential expression and gene set enrichment

For single-cell and spatial transcriptomic data, differential expression (DE) analysis was performed using the Seurat FindMarkers function on log-normalized data to identify overexpressed genes of indicated cell clusters or spatial regions. The MAST algorithm was used in DE analysis with log-fold change set to 0.25 and the "min.pct" parameter set to 0.1. For bulk RNA sequencing data, DE analysis was performed using DESeq2 v1.40.2 according to the recommended workflow. The upregulated genes were defined as log-fold change > 1 and adjusted $p < 0.05$.

For the calculation of gene set enrichment, indicated gene sets were derived from the MSigDB database, and the gene set overrepresentation was determined using the hypergeometric test with the ClusterProfiler v4.9.0 R package.

GSEA analysis

The indicated GO or KEGG signatures were derived from the MSigDB database, and the upregulated gene sets of oxLDL-treated TAMs or *Trem2*$^{-/-}$ TAMs from bulk RNA sequencing were obtained by DESeq2 analysis as described above. GSEA of signature genes was performed on the genes ranked by log-fold change between the indicated TAM subset and other TAMs, using ClusterProfiler v4.9.0. Gene signatures with FDR < 0.05 were considered significantly enriched.

Label transfer using a reference

To investigate the association between cancer cell archetypes and immunotherapy response, we transferred the archetype labels of cancer cells from the snRNA-seq dataset to the cancer cells in our neoadjuvant cohort. Briefly, cancer cells from ICB-R and ICB-NR HCC samples were first identified from hepatocyte-linage cells using inferCNV as described above. Then, transfer of cancer cell archetype labels was performed using the FindTransferAnchors and TransferData functions in Seurat v4.0.3, setting the archetype annotation generated from our snRNA-seq dataset as a reference. Expressions of cancer cell archetype-related markers were used to verify the accuracy of the transferred labels.

Alignment, quantification, and quality control of spatial transcriptomic data

For 10× Genomics Visium sequencing data, the raw reads were mapped to the human reference genome (refdata-gex-GRCh38-2020-A) using SpaceRanger software (v1.2.1, 10× Genomics). Briefly, Space Ranger showed the capture area of the organization in the chip by image processing algorithm and aligned reads of each spot according to the Spatial barcode information in Clean Data. Spot numbers, reads in spot, detected genes, and UMIs were counted. All spots detected by Space Ranger were included in the downstream analysis.

Identification of tumor and stromal regions in spatial transcriptomic data

To identify tumor and stromal regions in spatial transcriptomic data, we first clustered tissue spots following the recommended Seurat workflow. Briefly, gene expression matrices of tissue spots were normalized and scaled using the Seurat SCTransform function, followed by PCA analysis, neighborhood graph building, and clustering with the Louvain algorithm (resolution = 0.8). DE analysis was then performed using the Seurat FindAllMarkers function to find marker genes of each spatial cluster. The assignment of tumor and stromal region was based on the gene signatures and location of each spatial cluster: clusters that located in the cancer cells on H&E staining and upregulated hepatocyte-linage markers (*ALB, TTR, ALDH1A1* etc.) were defined as tumor regions, while clusters that located in the stromal cells on H&E staining and upregulated stromal-related markers (*COL1A1, COL1A2, TAGLN*, etc.) were defined as stromal regions.

Mapping single-cell data onto spatial sections

To spatially locate the cell types on the spatial transcriptomics sections, we utilized the anchor-based integration method in Seurat v4.0.3. Briefly, scRNA-seq or snRNA-seq data from HCC tumor samples were used as reference. We utilized the annotation labels obtained from subtype characterization of main cell linages, as shown in Fig. 2A. The reference scRNA-seq or snRNA-seq data were first normalized and scaled using the Seurat SCTransform function. Then, integration of spatial and single-cell data was performed using Seurat FindTransferAnchors and TransferData functions with default parameters. Each Visium section was analyzed separately. Results were visualized by the Seurat SpatialFeaturePlot function, and the plots represent estimated abundance for indicated cell types. To identify the co-localization pattern of TME cell types, Pearson correlation coefficients were calculated between the cell type compositions of all spots in the tumor region. To validate the spatial localization pattern revealed by the Seurat integration method, we used cell2location v0.1.4, a deep learning-based spatial deconvolution method, according to the recommended workflow[25], with all parameters set to default.

Estimation of metabolic flux and metabolites

We used FLUXestimator[38] to evaluate the metabolic flux activity and metabolite abundance on our spatial transcriptomic data according to the recommended workflow. The estimated metabolic flux and metabolite levels were visualized using the Seurat SpatialFeaturePlot function.

Histology quantifications

The quantifications of TREM2^{+}SPP1^{+} TAMs in human primary HCC, ICB-NR HCC, ICB-R HCC, or HCC TMA were performed using the inForm software package (Akoya Biosciences) as previously described[53]. Briefly, the images were first segmented into tumor and stroma tissue areas based on the staining pattern of DAPI. Individual cells were then segmented, and quantification of positive/negative cells was performed using the inForm active learning phenotyping algorithm by assigning different cell phenotypes across several fields that were representative of the whole scan. This quantification process was applied to the whole section to quantify all different cell types.

For the quantification of SQLE immunofluorescence intensity in ICB-NR or ICB-R HCC samples, 6 random fields were selected in each ICB-NR or ICB-R section. In each field, tumor and stromal regions were manually segmented, and the SQLE immunofluorescence intensity was measured using ImageJ software (National Institutes of Health). The mean fluorescence intensity of 6 fields was calculated as the intensity of the corresponding section. Then, the intensity of different sections was compared.

Bulk RNA sequencing analysis

RNA was isolated using TRIzol reagent. A total of 3 μg RNA per sample was used as input for the sequencing library preparations, which were then sequenced on an Illumina Novaseq6000 platform with 150 bp paired-end reads generated. The experimental procedures were performed by Jiayin Biotechnology Ltd. (Shanghai, China). Each sample group contained at least 2 biological replicates. The alignment and quantification of raw reads were performed by STAR v2.7.10 and HTSeq v0.6.0. Then, we applied the DESeq2 algorithm for normalization of expression matrices and DE analysis as described above.

Scoring signatures on single-cell or bulk RNA-seq data

For scoring TAM signatures on single-cell data, the Seurat AddModuleScore function was used, and the top 50 genes ranked by log-fold change were considered as the signatures of the corresponding TAM subsets. For scoring gene signatures on bulk RNA-seq data, we utilized the GSVA algorithm with the parameter "kcdf" set to "Poisson" if it was scoring on raw counts, and with the parameter "kcdf" set to "Gaussian" if it was scoring on normalized matrices. All TAM subset signatures, lipid peroxidation signatures, cholesterol metabolism signatures, and Scissor$^+$ signatures that were generated in this study were listed in Supplementary Data 3.

Cell type deconvolution of TCGA-LIHC samples

To estimate the indicated cell type proportion in TCGA-LIHC samples, we used BayesPrism v2.0 to deconvolute cell fractions using our annotated scRNA-seq or snRNA-seq data as reference. TCGA-LIHC expression data were downloaded from the GDC data portal.

Prediction of single-cell myeloid populations associated with survival

We used Scissor v2.0.0 to identify myeloid cell subpopulations in our human single-cell data that are significantly associated with worse patient survival (Scissor$^+$ cells) or better patient survival (Scissor$^-$ cells). Briefly, TCGA-LIHC survival and expression data were downloaded from the GDC data portal. Then, Scissor was used to construct a logistic regression model using the binary outcome of deceased vs. censored/alive, with the alpha parameter set to 0.01 and all other parameters set to default.

Survival analysis

We performed survival analyses to examine the clinical relevance of the expression of TREM2 and SPP1, the expression of 73 metabolism archetype-specific genes, or the BayesPrism-inferred fraction of TREM2$^+$TAM and metabolism archetype cancer cells. Briefly, deconvolution of cell types was performed as described above, and gene expressions were normalized using the TCGAanalyze_Normalization function from the TCGAbiolinks R package (v 2.34.0). Next, the samples were stratified into groups based on the optimal cut points predicted by the surv_cutpoint function (survminer v0.4.9) for the grouping signatures. Survival curves of the indicated groups of patients were estimated by the Kaplan–Meier method, with statistical significance calculated with log log-rank test. For the survival analysis of 73 metabolism archetype-specific genes, a univariate Cox proportional hazard model was constructed to calculate the hazard ratio for each gene.

We used the multivariate Cox proportional hazard model to examine the association of patient survival with clinical features and signatures of myeloid subclusters. Briefly, the top 50 genes ranked by log-fold change were considered as the signatures of the corresponding myeloid clusters (excluding cycling cells), and scoring of signatures was performed as described above. Then, patient pathological stage, sex, age, and myeloid cluster signatures were included to construct the multivariate Cox survival model (Pathological Stage: Stage I = 1, Stage II = 2, Stage III = 3; Sex: 'Male' = 1, 'Female' = 2; Age at diagnosis; Signature scores: below lower quantile = =1, between lower and upper quantile = 2, above upper quantile = 3). The Kaplan–Meier estimator, log-rank test, and Cox proportional hazard models were calculated by the survival R package (v3.5-5).

Statistical analysis

For all comparisons between two groups of independent datasets, a two-tailed unpaired *t*-test or Wilcoxon rank-sum test was performed, and the *p*-value and standard deviation of the mean (SD) were calculated. For all comparisons among more than two groups, one-way or two-way ANOVA followed by multiple comparisons was performed. The PFS, DFS, or OR were univariately analyzed by the Kaplan-Meier method, and statistical testing was performed using log log-rank test. The hazard ratio (HR) and confidence interval (95% CI) were computed using the univariate or multivariate Cox proportional hazard model. All statistical analysis was conducted either using GraphPad Prism v9.4.1 (GraphPad Software) or R v4.3.0 (R project). All the in vitro experiments were independently repeated at least three times (with at least three biological repeats in total), and the in vivo experiments included at least six biological repeats with a similar time course and treatment. Representative data from experiments performed at least in triplicate are shown.

Reporting summary

Further information on research design is available in the Nature Portfolio Reporting Summary linked to this article.

Data availability

The raw and processed human scRNA-seq data generated in this study have been deposited in the National Center for Biotechnology Information's Gene Expression Omnibus (GEO) database repository under accession number SRP374575 and GSE202642. The raw and processed human snRNA-seq, spatial transcriptomic sequencing and bulk RNA-seq data generated in this study have been deposited in the Genome Sequence Archive (GSA) database under accession code HRA011756, HRA011834, HRA011807 (raw), and OMIX010442, OMIX010476, OMIX010473 (processed). The raw and processed mouse scRNA-seq and bulk RNA-seq data have been deposited in the GSA database under the accession number CRA026592, CRA026515 (raw) and OMIX010443, OMIX010473 (processed). The human snRNA-seq and spatial transcriptomic sequencing data are available under restricted access because of data privacy and supervision. Researchers could send data requests for scientific purposes via the website [https://ngdc.cncb.ac.cn/gsa-human/] after registration. Data access requests will be processed within one month by following the guidelines for Genome Sequence Archive for noncommercial use. Once access has been approved, the data will be available for one month. Previously published data used in this study are available under accession codes: GSE149614 [GEO: https://www.ncbi.nlm.nih.gov/geo/query/acc.cgi?acc=GSE149614], GSE14520 [GEO: https://www.ncbi.nlm.nih.gov/geo/query/acc.cgi?acc=gse14520], GSE124751 [GEO: https://www.ncbi.nlm.nih.gov/geo/query/acc.cgi?acc=GSE124751], GSE97098 [GEO: https://www.ncbi.nlm.nih.gov/geo/query/acc.cgi?acc=GSE97098], GSE151710 [GEO: https://www.ncbi.nlm.nih.gov/geo/query/acc.cgi?acc=GSE151710], GSE224411 [GEO: https://www.ncbi.nlm.nih.gov/geo/query/acc.cgi?acc=GSE224411], GSE235863 [GEO: https://www.ncbi.nlm.nih.gov/geo/query/acc.cgi?acc=GSE235863], TCGA-LIHC [TCGA database: https://www.cancer.gov/tcga], LIRI-JP [ICGC database: https://dcc.icgc.org/], OPE000321 [biosino NODE database: https://www.biosino.org/node/project/detail/OEP000321] and skrx2fz79n [Mendeley database: https://data.mendeley.com/datasets/skrx2fz79n/1]. The remaining data are available within the Article, Supplementary Information Source Data file or from the corresponding author on request. Source data are provided with this paper.

Code availability

The bioinformatic analysis code has been uploaded into the github (https://github.com/Cthfudan/hcc). The codes used in this study have been uploaded to Zenodo and are freely available at: https://doi.org/10.5281/zenodo.15618831[75].

References

1. Samant, H., Amiri, H. S. & Zibari, G. B. Addressing the worldwide hepatocellular carcinoma: epidemiology, prevention and management. *J. Gastrointest. Oncol.* **12**, S361–s373 (2021).
2. Siegel, R. L., Miller, K. D., Fuchs, H. E. & Jemal, A. Cancer statistics, 2022. *CA Cancer J. Clin.* **72**, 7–33 (2022).
3. Vitale, I., Shema, E., Loi, S. & Galluzzi, L. Intratumoral heterogeneity in cancer progression and response to immunotherapy. *Nat. Med.* **27**, 212–224 (2021).
4. Li, X. Y., Shen, Y., Zhang, L., Guo, X. & Wu, J. Understanding initiation and progression of hepatocellular carcinoma through single cell sequencing. *Biochim. Biophys. Acta Rev. Cancer* **1877**, 188720 (2022).
5. Slyper, M. et al. A single-cell and single-nucleus RNA-Seq toolbox for fresh and frozen human tumors. *Nat. Med.* **26**, 792–802 (2020).
6. Wen, F., Tang, X., Xu, L. & Qu, H. Comparison of single-nucleus and single-cell transcriptomes in hepatocellular carcinoma tissue. *Mol. Med. Rep.* **26**, 339 (2022).
7. Hou, Y. et al. Single-cell triple omics sequencing reveals genetic, epigenetic, and transcriptomic heterogeneity in hepatocellular carcinomas. *Cell Res.* **26**, 304–319 (2016).
8. Zheng, H. et al. Single-cell analysis reveals cancer stem cell heterogeneity in hepatocellular carcinoma. *Hepatology* **68**, 127–140 (2018).
9. de Visser, K. E. & Joyce, J. A. The evolving tumor microenvironment: From cancer initiation to metastatic outgrowth. *Cancer Cell* **41**, 374–403 (2023).
10. Kao, K. C., Vilbois, S., Tsai, C. H. & Ho, P. C. Metabolic communication in the tumour-immune microenvironment. *Nat. Cell Biol.* **24**, 1574–1583 (2022).
11. Di Conza, G. et al. Tumor-induced reshuffling of lipid composition on the endoplasmic reticulum membrane sustains macrophage survival and pro-tumorigenic activity. *Nat. Immunol.* **22**, 1403–1415 (2021).
12. Raines, L. N. et al. PERK is a critical metabolic hub for immunosuppressive function in macrophages. *Nat. Immunol.* **23**, 431–445 (2022).
13. Colonna, M. The biology of TREM receptors. *Nat. Rev. Immunol.* **23**, 580–594 (2023).
14. Molgora, M. et al. TREM2 modulation remodels the tumor myeloid landscape enhancing anti-PD-1 immunotherapy. *Cell* **182**, 886–900.e817 (2020).
15. Sun, R. et al. Neutral ceramidase regulates breast cancer progression by metabolic programming of TREM2-associated macrophages. *Nat. Commun.* **15**, 966 (2024).
16. Tan, J. et al. TREM2(+) macrophages suppress CD8(+) T-cell infiltration after transarterial chemoembolisation in hepatocellular carcinoma. *J. Hepatol.* **79**, 126–140 (2023).
17. Sharma, A. et al. Onco-fetal reprogramming of endothelial cells drives immunosuppressive macrophages in hepatocellular carcinoma. *Cell* **183**, 377–394.e321 (2020).
18. Zhu, G. Q. et al. CD36(+) cancer-associated fibroblasts provide immunosuppressive microenvironment for hepatocellular carcinoma via secretion of macrophage migration inhibitory factor. *Cell Discov.* **9**, 25 (2023).
19. Wang, S. S. et al. Perivenous stellate cells are the main source of myofibroblasts and cancer-associated fibroblasts formed after chronic liver injuries. *Hepatology* **74**, 1578–1594 (2021).
20. Filliol, A. et al. Opposing roles of hepatic stellate cell subpopulations in hepatocarcinogenesis. *Nature* **610**, 356–365 (2022).
21. Xu, C. et al. Probabilistic harmonization and annotation of single-cell transcriptomics data with deep generative models. *Mol. Syst. Biol.* **17**, e9620 (2021).
22. Luecken, M. D. et al. Benchmarking atlas-level data integration in single-cell genomics. *Nat. Methods* **19**, 41–50 (2022).
23. Trapnell, C. Defining cell types and states with single-cell genomics. *Genome Res.* **25**, 1491–1498 (2015).
24. Hao, Y. et al. Integrated analysis of multimodal single-cell data. *Cell* **184**, 3573–3587.e3529 (2021).
25. Kleshchevnikov, V. et al. Cell2location maps fine-grained cell types in spatial transcriptomics. *Nat. Biotechnol.* **40**, 661–671 (2022).
26. Huang, Y., Hong, W. & Wei, X. The molecular mechanisms and therapeutic strategies of EMT in tumor progression and metastasis. *J. Hematol. Oncol.* **15**, 129 (2022).
27. Enyedi, B., Jelcic, M. & Niethammer, P. The cell nucleus serves as a mechanotransducer of tissue damage-induced inflammation. *Cell* **165**, 1160–1170 (2016).
28. Chu, T., Wang, Z., Pe'er, D. & Danko, C. G. Cell type and gene expression deconvolution with BayesPrism enables Bayesian integrative analysis across bulk and single-cell RNA sequencing in oncology. *Nat. Cancer* **3**, 505–517 (2022).
29. Liu, Y. et al. Identification of a tumour immune barrier in the HCC microenvironment that determines the efficacy of immunotherapy. *J. Hepatol.* **78**, 770–782 (2023).
30. Sun, D. et al. Identifying phenotype-associated subpopulations by integrating bulk and single-cell sequencing data. *Nat. Biotechnol.* **40**, 527–538 (2022).
31. Pang, X. et al. Osteopontin as a multifaceted driver of bone metastasis and drug resistance. *Pharm. Res.* **144**, 235–244 (2019).
32. Wang, L. & Niu, X. Immunoregulatory roles of osteopontin in diseases. *Nutrients* **16** (2024).
33. Klement, J. D. et al. An osteopontin/CD44 immune checkpoint controls CD8+ T cell activation and tumor immune evasion. *J. Clin. Invest.* **128**, 5549–5560 (2018).
34. Eun, J. W. et al. Cancer-associated fibroblast-derived secreted phosphoprotein 1 contributes to resistance of hepatocellular carcinoma to sorafenib and lenvatinib. *Cancer Commun. (Lond.)* **43**, 455–479 (2023).
35. Vredevoogd, D. W. et al. Augmenting immunotherapy impact by lowering tumor TNF cytotoxicity threshold. *Cell* **178**, 585–599.e515 (2019).
36. Sun, Y. et al. Targeting TBK1 to overcome resistance to cancer immunotherapy. *Nature* **615**, 158–167 (2023).
37. Greten, F. R. & Grivennikov, S. I. Inflammation and cancer: triggers, mechanisms, and consequences. *Immunity* **51**, 27–41 (2019).
38. Zhang, Z. et al. FLUXestimator: a webserver for predicting metabolic flux and variations using transcriptomics data. *Nucleic Acids Res.* **51**, W180–w190 (2023).
39. Jaitin, D. A. et al. Lipid-associated macrophages control metabolic homeostasis in a Trem2-dependent manner. *Cell* **178**, 686–698.e614 (2019).
40. Prendeville, H. & Lynch, L. Diet, lipids, and antitumor immunity. *Cell Mol. Immunol.* **19**, 432–444 (2022).
41. Yang, H. et al. Pharmacogenomic profiling of intra-tumor heterogeneity using a large organoid biobank of liver cancer. *Cancer Cell* **42**, 535–551.e538 (2024).
42. Yang, W. S. & Stockwell, B. R. Ferroptosis: death by lipid peroxidation. *Trends Cell Biol.* **26**, 165–176 (2016).
43. Chen, X. et al. Tumor suppressor CEBPA interacts with and inhibits DNMT3A activity. *Sci. Adv.* **8**, eabl5220 (2022).
44. Gill, S., Stevenson, J., Kristiana, I. & Brown, A. J. Cholesterol-dependent degradation of squalene monooxygenase, a control

point in cholesterol synthesis beyond HMG-CoA reductase. *Cell Metab.* **13**, 260–273 (2011).
45. Gao, Q. et al. Integrated proteogenomic characterization of hbv-related hepatocellular carcinoma. *Cell* **179**, 561–577.e522 (2019).
46. Wang, T. et al. Integrating bulk and single-cell RNA sequencing reveals cellular heterogeneity and immune infiltration in hepatocellular carcinoma. *Mol. Oncol.* **16**, 2195–2213 (2022).
47. Lee, S. H. et al. Consensus subtypes of hepatocellular carcinoma associated with clinical outcomes and genomic phenotypes. *Hepatology* **76**, 1634–1648 (2022).
48. Su, P. et al. Enhanced lipid accumulation and metabolism are required for the differentiation and activation of tumor-associated macrophages. *Cancer Res.* **80**, 1438–1450 (2020).
49. Yang, Z. et al. Cancer cell-intrinsic XBP1 drives immunosuppressive reprogramming of intratumoral myeloid cells by promoting cholesterol production. *Cell Metab.* **34**, 2018–2035.e2018 (2022).
50. Patterson, M. T. et al. Trem2 promotes foamy macrophage lipid uptake and survival in atherosclerosis. *Nat. Cardiovasc. Res.* **2**, 1015–1031 (2023).
51. Ma, L. et al. Single-cell atlas of tumor cell evolution in response to therapy in hepatocellular carcinoma and intrahepatic cholangiocarcinoma. *J. Hepatol.* **75**, 1397–1408 (2021).
52. Wang, H. et al. Antiandrogen treatment induces stromal cell reprogramming to promote castration resistance in prostate cancer. *Cancer Cell* **41**, 1345–1362.e1349 (2023).
53. Bill, R. et al. CXCL9:SPP1 macrophage polarity identifies a network of cellular programs that control human cancers. *Science* **381**, 515–524 (2023).
54. Chen, Z., Han, F., Du, Y., Shi, H. & Zhou, W. Hypoxic microenvironment in cancer: molecular mechanisms and therapeutic interventions. *Signal Transduct. Target Ther.* **8**, 70 (2023).
55. Donadon, M. et al. Macrophage morphology correlates with single-cell diversity and prognosis in colorectal liver metastasis. *J. Exp. Med.* **217**, e20191847 (2020).
56. Ma, X. et al. Cholesterol Induces CD8(+) T Cell Exhaustion in the Tumor Microenvironment. *Cell Metab.* **30**, 143–156.e145 (2019).
57. Liu, D. et al. Squalene epoxidase drives NAFLD-induced hepatocellular carcinoma and is a pharmaceutical target. *Sci. Transl. Med.* **10**, eaap9840 (2018).
58. Xu, R. et al. SQLE promotes pancreatic cancer growth by attenuating ER stress and activating lipid rafts-regulated Src/PI3K/Akt signaling pathway. *Cell Death Dis.* **14**, 497 (2023).
59. Abdel-Rahman, S. M. & Nahata, M. C. Oral terbinafine: a new antifungal agent. *Ann. Pharmacother.* **31**, 445–456 (1997).
60. Ruiz de Galarreta, M. et al. β-Catenin Activation Promotes Immune Escape and Resistance to Anti-PD-1 Therapy in Hepatocellular Carcinoma. *Cancer Discov.* **9**, 1124–1141 (2019).
61. Nguyen, T., Du, J. & Li, Y. C. A protocol for macrophage depletion and reconstitution in a mouse model of sepsis. *STAR Protoc.* **2**, 101004 (2021).
62. Sullivan, M. R. et al. Quantification of microenvironmental metabolites in murine cancers reveals determinants of tumor nutrient availability. *Elife* **8**, e44235 (2019).
63. Fleming, S. J. et al. Unsupervised removal of systematic background noise from droplet-based single-cell experiments using CellBender. *Nat. Methods* **20**, 1323–1335 (2023).
64. Sun, Y. et al. Single-cell landscape of the ecosystem in early-relapse hepatocellular carcinoma. *Cell* **184**, 404–421.e416 (2021).
65. Korsunsky, I. et al. Fast, sensitive and accurate integration of single-cell data with Harmony. *Nat. Methods* **16**, 1289–1296 (2019).
66. Azizi, E. et al. Single-cell map of diverse immune phenotypes in the breast tumor microenvironment. *Cell* **174**, 1293–1308.e1236 (2018).
67. Zheng, L. et al. Pan-cancer single-cell landscape of tumor-infiltrating T cells. *Science* **374**, abe6474 (2021).
68. Gonzalez, H. et al. Cellular architecture of human brain metastases. *Cell* **185**, 729–745.e720 (2022).
69. Puram, S. V. et al. Single-cell transcriptomic analysis of primary and metastatic tumor ecosystems in head and neck cancer. *Cell* **171**, 1611–1624.e1624 (2017).
70. Biermann, J. et al. Dissecting the treatment-naive ecosystem of human melanoma brain metastasis. *Cell* **185**, 2591–2608.e2530 (2022).
71. Miao, G. et al. From degenerative disease to malignant tumors: Insight to the function of ApoE. *Biomed. Pharmacother.* **158**, 114127 (2023).
72. Webb, N. R. High-density lipoproteins and serum amyloid A (SAA). *Curr. Atheroscler. Rep.* **23**, 7 (2021).
73. Xu, H., Niu, M., Yuan, X., Wu, K. & Liu, A. CD44 as a tumor biomarker and therapeutic target. *Exp. Hematol. Oncol.* **9**, 36 (2020).
74. Garcia-Alonso, L. et al. Single-cell roadmap of human gonadal development. *Nature* **607**, 540–547 (2022).
75. Chu, T. et al. Metabolism archetype cancer cells induce protumor TREM2+ macrophages via oxLDL-mediated metabolic interplay in hepatocellular carcinoma. *Zenodo* https://doi.org/10.5281/zenodo.15618831 (2025).

Acknowledgements

This project was supported by grants from the National Natural Science Foundation of China (No. 81773067, 82073217, 82073218, and 82003084), National Key Research and Development Program of China (2018YFC1312100), Shanghai Municipal Science and Technology Major Project (Grant No. 2018SHZDZX05) and Shanghai Municipal Key Clinical Specialty, CAMS Innovation Fund for Medical Sciences (CIFMS) (2019-I2M-5-058). We also thank Berry Genomics Corporation for performing single-cell RNA sequencing and spatial transcriptomic sequencing, and Shanghai Biochip Corporation for performing single-nucleus RNA sequencing.

Author contributions

Y.S., D.Y., W.L, T.C., and G.Z. designed the experiment and prepared the manuscript. T.C., G.Z., and W.Q. performed most in vitro experiments. T.C., G.Z. and Z.T. contributed to the statistical analysis. T.C., R.Y. and W.Q. performed the animal experiments. Z.T., H.P., Y.W., R.T., L.C., Z.G., Y.B., Q.Z., J.C., S.M., Y.F., J.G. and X.W. performed a subset of the experiments, which were supervised by J.Z., W.L., J.F., D.Y., and Y.S.

Competing interests

The authors declare no competing interests.

Additional information

Supplementary information The online version contains supplementary material available at https://doi.org/10.1038/s41467-025-62132-y.

Correspondence and requests for materials should be addressed to Weiren Liu, Dan Ye, Jia Fan or Yinghong Shi.

Peer review information *Nature Communications* thanks Defne Bayik, who co-reviewed with Oriana Teran Pumar and the other, anonymous, reviewer(s) for their contribution to the peer review of this work. A peer review file is available.